Double adjustment of Co and Sr in LaMnO$_{3+\delta}$ perovskite oxygen carriers for chemical looping steam methane reforming

Xianglei Yin [a,b], Laihong Shen [a,*], Shen Wang [a], Baoyi Wang [a], Cheng Shen [a]

[a] Key Laboratory of Energy Thermal Conversion and Control of Ministry of Education, School of Energy and Environment, Southeast University, Nanjing 210096, China
[b] School of Mechanical and Electronic Engineering, Zaozhuang University, Zaozhuang 277160, China

ABSTRACT

As a key factor for chemical looping steam methane reforming, the oxygen carrier with high quality is essential. In this work, both high reactivity and coking resistance of the La$_{1-x}$Sr$_x$Mn$_{1-y}$Co$_y$O$_{3+\delta}$ oxygen carriers are achieved by double adjustment of Co and Sr. The redox tests and characterization results showed that the introduction of cobalt provided surface active sites to accelerate the activation of methane on the surface, and the Sr doping increased the oxygen vacancies which facilitated the migration of oxygen anion in the bulk of the oxygen carrier particles. The doping of Co and Sr can match the supply of oxygen from the bulk and the need of oxygen on the surface of the oxygen carrier particles. The best substitution proportion of Co and Sr could be set in range of 0.4–0.5 and 0.2–0.4, respectively. The La$_{0.8}$Sr$_{0.2}$Mn$_{0.5}$Co$_{0.5}$O$_{3+\delta}$ exhibited satisfactory performance and good stability in the cyclic redox tests.

1. Introduction

Methane is the main constituent of natural gas and shale gas which possess an abundant reserve and an increasing yield [1]. Compared with the direct conversion of methane into chemicals such as C2 and heavy hydrocarbons, the reforming of methane into syngas is a low-energy and high-efficiency way of methane utilization [2,3]. The syngas could be used as feedstock to produce chemicals and liquid fuels by Fischer-Tropsch (F-T) synthesis. Up to now, methane reforming is almost entirely carried out by steam methane reforming (SMR) (R1) in the industry [4].

$$CH_4 + H_2O \rightarrow CO + 3H_2 \tag{R1}$$

However, the downstream F-T synthesis requires the molar ratio of H$_2$/CO of 2. The syngas produced from R1 needs to be further processed or the composite reforming process should be adopted to adjust the ratio of H$_2$/CO, which results in large energy consumption and equipment investment.

On the other hand, hydrogen is a clean and environmentally friendly energy with a high calorific value [5], and also is an important chemical feedstock [6,7]. Industrial hydrogen generation is mainly through SMR (R1) and the syngas produced from R1 needs to be processed by means

of water-gas shift reaction (R2) for subsequent purification of hydrogen [8].

$$CO + H_2O \rightarrow CO_2 + H_2 \tag{R2}$$

The additional steps of gas separation and hydrogen purification cause high energy consumption and low efficiency [5,9].

Chemical looping steam methane reforming (CLSMR) is a novel technology to accomplish the reforming of methane into syngas and generation of hydrogen from water synchronously. As depicted in Fig. 1, CLSMR divides the SMR process into two steps: a methane conversion stage and a water splitting stage. The oxygen carrier, which usually employs a metal oxide, transfers lattice oxygen from steam to methane [10,11]. Methane is selectively oxidized into syngas by the lattice oxygen from oxygen carriers (MeO$_x$) in the methane conversion stage (R3). The reduced oxygen carriers (MeO$_{x-y}$) are then oxidized by steam to replenish its lattice oxygen and generate hydrogen in the water splitting stage (R4).

$$MeO_x + yCH_4 \rightarrow MeO_{x-y} + 2yH_2 + yCO \tag{R3}$$

$$MeO_{x-y} + yH_2O \rightarrow MeO_x + yH_2 \tag{R4}$$

The development and improvement of oxygen carriers is an

---

* Correspondence to: Key Laboratory of Energy Thermal Conversion and Control of Ministry of Education, Southeast University, No. 2 Sipailou Road, Nanjing, Jiangsu 210096, China.
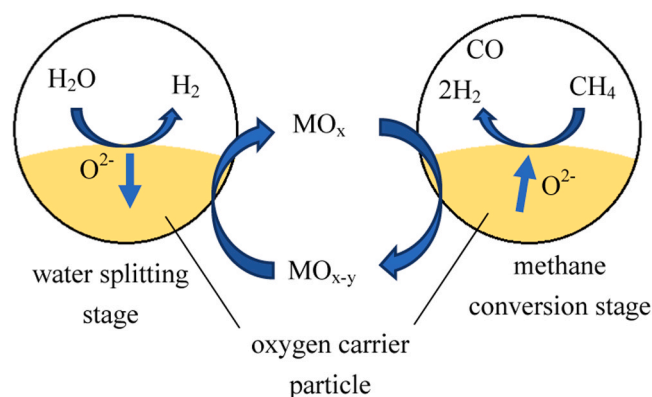*E-mail address:* lhshen@seu.edu.cn (L. Shen).

Fig. 1. Schematic of co-production of syngas and hydrogen through CLSMR.

important issue for chemical looping system and the success of CLSMR process is highly dependent on suitable oxygen carriers. Desired oxygen carriers of CLSMR should have sufficiently high reactivity to ensure the methane conversion, superior selectivity towards syngas, excellent oxygen storage capacity (OSC) to achieve a high yield of syngas and hydrogen, good stability under alternating redox process, negligible carbon deposition, eligible mechanical property and agglomeration (sintering) resistance at high temperatures. However, the suitable oxygen carriers for CLSMR are very limited. As far as we know, perovskite-type oxides with rare earth metals are the most applicable oxygen carriers for CLSMR.

The perovskite oxides have excellent oxygen anion conductivity [12,13] and good thermal stability [14]. The redox properties of perovskite could be tailored through partial substituting the metal cations and adjusting the substitution proportion [15]. $LaFeO_3$-based perovskites have received extensive attention and lots of study investigated the performance of $LaFeO_3$ [16], $La_{1-x}Sr_xFeO_3$ [17], $LaFe_{1-x}Co_xO_3$ [4], $LaFe_{1-x}Ni_xO_3$ [18], $La_{1-x}Sr_xM_yFe_{1-y}O_3$ (M=Cr, Co, Ni, Cu) [19,20] and $La_{1.6}Sr_{0.4}FeCoO_6$ [11] in CLSMR application. These $LaFeO_3$-based perovskites own high reactivity of redox reaction attributed to their superior oxygen conduction and large concentrations of oxygen vacancies in the structure.

Although the Fe-Ce oxide and $LaFeO_3$-based perovskites exhibited good performance for CLSMR, carbon deposition is still an insurmountable problem [21]. Carbon deposition originates from the methane cracking reaction (R5) which occurred in the late period of the methane conversion stage.

$$CH_4 \rightarrow C + 2H_2 \tag{R5}$$

Methane cracking reaction produces superfluous hydrogen leading to higher H_2/CO and worsening the syngas quality in the methane conversion stage. During the water splitting stage, the carbon is oxidized into CO and CO_2 through the water gas reaction (R6) and the water gas shift reaction (R2), which brings in impurities in hydrogen and lowers the hydrogen purity in the water splitting stage.

$$C + H_2O \rightarrow CO + H_2 \tag{R6}$$

The reason for the carbon deposition is that Fe, Co and Ni atoms or cations can facilitate the activation and cracking of methane. The activated methane would form deposited carbon if the conduction rate of oxygen anion was unable to keep up the rate with the activation and cracking of methane. In other words, carbon formation occurs in case of that the supply of the available oxygen from the internal is not sufficient enough to match the need of oxygen on the surface of the oxygen carrier particles. For the $LaFeO_3$-based perovskites, a large amount of iron provides active sites for methane activation and cracking. Although the reactivity of methane reforming is improved, the number of the Fe active sites is difficult to adjust to match the oxygen supply, resulting in carbon

deposition. $LaMnO_{3+\delta}$ perovskite does not contain highly active sites for methane cracking, which do not cause carbon deposition but lead to low reactivity. According to our previous work [22], Co active site is more efficient and easier to regulate the reactivity than Fe for the $LaMnO_{3+\delta}$ perovskite. In this work, the $LaMnO_{3+\delta}$ perovskite was used as a matrix structure, Co was doped to regulate the number of active sites for methane activation in the surface of oxygen carrier and Sr doping was adopted to accelerate the migration rate of oxygen in the bulk. The double adjustment of Co and Sr was beneficial to accomplish the matching of the transmission rate of oxygen ion in the interior and the activation rate of methane on the surface of the oxygen carriers, which ensured both high reactivity and resistance towards carbon formation.

2. Experimental

2.1. Preparation of the perovskites

9 $La_{1-x}Sr_xMn_{1-y}Co_yO_{3+\delta}$ perovskites are investigated in this work, including $LaMnO_{3+\delta}$ perovskite, 4 $LaMn_{1-y}Co_yO_{3+\delta}$ perovskites (y=0.1, 0.3, 0.4, 0.5), 3 $La_{1-x}Sr_xMn_{0.5}Co_{0.5}O_{3+\delta}$ perovskites (x=0.2, 0.3, 0.4) as well as $La_{0.8}Sr_{0.2}Mn_{0.7}Co_{0.3}O_{3+\delta}$ perovskite. All these perovskites were prepared through a sol-gel method. The precursor $La(NO_3)_3 \cdot 6H_2O$ (AR), $Sr(NO_3)_2$ (AR), $Mn(NO_3)_2$ (50 wt% in solution), $Co(NO_3)_2 \cdot 6H_2O$ (99.99%) and citric acid (AR) was dissolved in deionized water with molar ratio of 1.5:1 for citric acid and the total metal cations. Then ethylene glycol (AR) at the molar ratio of 1:1 with respect to citric acid was added to the nitrate and citric solution. After fully mixing, the aqueous ammonia (AR) was added into the mixture drop by drop till the pH of the solution rising to eight. The mixed solution was evaporated by magnetic stirring at 80 °C till a wet transparent gel was formed. The wet gel was dried at 110 °C for 24 h to form a xerogel. Then the xerogel was transferred to a muffle oven and then suffered a decomposition at 350 °C for 2 h and a calcination at 850 °C for 2 h to generate perovskite powders.

2.2. Oxygen carriers characterization

X-ray diffraction (XRD) was conducted on a X-ray diffractometer (SmartLab, Rigaku) equipped with Cu Kα radiation (*U*=40 kV, *I*=30 mA). The scanned range of 2θ was set from 10° to 90° with the step rate of $0.1° \cdot s^{-1}$.

X-ray photoelectron spectroscopy (XPS) was performed on an apparatus (Thermo ESCALAB250, USA) using a monochromatic Al Kα X-ray (*hν*=1486.6 eV). The binding energy was calibrated through fixing the peak of the adventitious carbon to 284.8 eV in the spectra of C 1s

Hydrogen temperature programmed reduction (H_2-TPR) was carried out on the Quantachrome system, the reduction was performed in 10% H_2/Ar with the flow rate of 30 mL min^{-1} and in the temperature range of 50–900 °C with the heating rate of 10 °C min^{-1}.

CH_4 temperature programmed reduction (CH_4-TPR) was conducted in a miniature fixed-bed reactor system and the exhaust gases were analyzed by an online mass spectrometer (Hiden Analytical Co., England). 50 mg oxygen carriers were reduced in 5% CH_4/Ar with a flow rate of 30 mL min^{-1} and the temperature increased from 300 °C to 900 °C with a heating rate of 10 °C min^{-1}.

Electron paramagnetic resonance (EPR) was performed on a Bruker A300 spectrometer. The magnetic field possessed the center field at 3510 G with a sweep width of 100 G.

Scanning electron microscope (SEM) was conducted using an Ultra Plus microscope (Carl Zeiss AG).

2.3. Redox tests

The evaluation of CLSMR performance was carried out in a fixed-bed reactor which fitted a quartz tube vertically in a programmable electric furnace. The quartz tube was manufactured with an inner diameter of
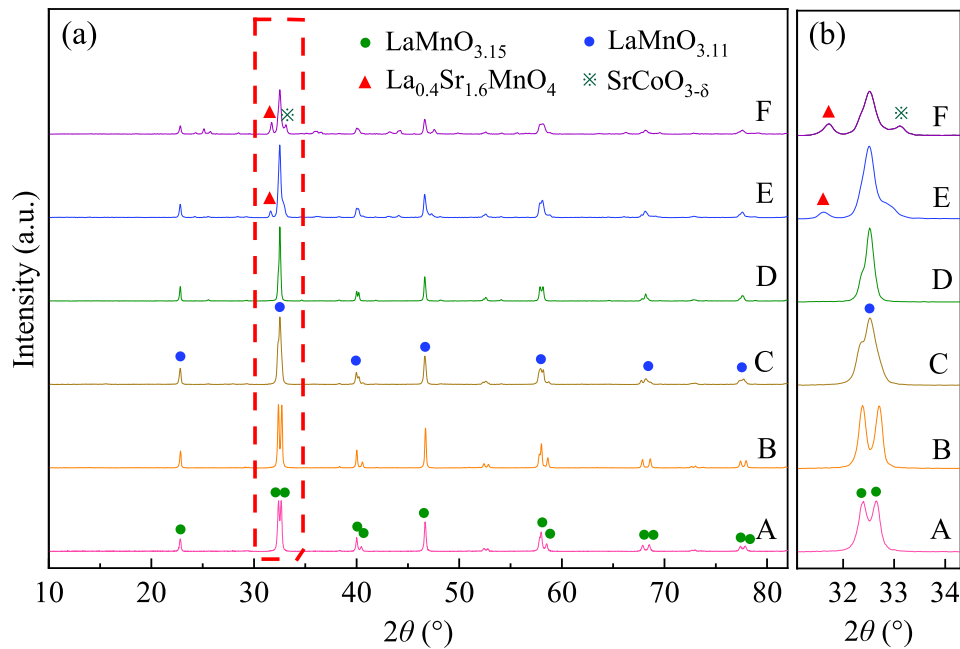
Fig. 2. XRD patterns of fresh LaMnO$_{3+\delta}$(A), LaMn$_{0.9}$Co$_{0.1}$O$_{3+\delta}$(B), LaMn$_{0.7}$Co$_{0.3}$O$_{3+\delta}$(C), LaMn$_{0.5}$Co$_{0.5}$O$_{3+\delta}$(D), La$_{0.8}$Sr$_{0.2}$Mn$_{0.5}$Co$_{0.5}$O$_{3+\delta}$(E), La$_{0.6}$Sr$_{0.4}$Mn$_{0.5}$Co$_{0.5}$O$_{3+\delta}$(F). ((b) is the enlargement of the dashed box in (a)). (For interpretation of the references to colour in this figure legend, the reader is referred to the web version of this article.).

19 mm and a height of 600 mm.

The methane conversion stage and water splitting stage were both conducted at 850 °C under atmospheric pressure with 2 g oxygen carrier sample. The methane conversion stage was performed by injecting 5% CH$_4$/N$_2$ with the total flow rate of 240 mL min^{-1} for 20 min. In the water splitting stage, steam was introduced into the reactor mixed with N$_2$ for 30 min. The flow rate of N$_2$ was 240 mL min^{-1} and that of steam was set to 0.1 g min^{-1}. The outlet gas was detected by a gas analyzer (MRU-VARIO PLUS, Germany). For the cyclic tests of La$_{0.8}$Sr$_{0.2}$Mn$_{0.5}$Co$_{0.5}$O$_{3+\delta}$, the methane conversion stage was conducted for 12 min to avoid the carbon deposition period, and pure N$_2$ with flow rate of 240 mL min^{-1} flowed through the reactor to purge the residual methane, steam and produced gas after each methane conversion stage and water splitting stage.

2.4. Calculation of property parameters

In the methane conversion stage, the total yield of each outlet gas (N_i, mmol g^{-1}) can be calculated by:

$$N_i = \int_0^{(\tau_1+\tau_2)} n_i d\tau \tag{E1}$$

where n_i is the molar flow rate of each outlet gas (mmol min^{-1} g^{-1}), i refers to CO$_2$, CO, H$_2$, CH$_4$ in the outlet gas, τ_1 and τ_2 is the time when the methane reforming period and the carbon deposition period ends (min).

The yield of each gas generated in the methane reforming period ($N_{i, MR}$, mmol g^{-1}) and carbon deposition period ($N_{i,CD}$, mmol g^{-1}) be calculated by:

$$N_{i,MR} = \int_0^{\tau_1} n_i d\tau \tag{E2}$$

$$N_{i,CD} = \int_{\tau_1}^{\tau_2} n_i d\tau \tag{E3}$$

where τ_1 and τ_2 are the time when the methane reforming period and the carbon deposition period end (min).

The methane conversion (X_{CH4}, %) is

$$X_{CH_4} = (N_{CH_4,in} - N_{CH_4,out})/N_{CH_4,in} \times 100\% \tag{E4}$$

the CO selectivity (S_{CO}, %) is:

$$S_{CO} = N_{CO}/(N_{CO} + N_{CO_2}) \times 100\% \tag{E5}$$

the molar ratio of H$_2$ to CO is:

$$H_2/CO = N_{H_2}/N_{CO} \tag{E6}$$

the amount of carbon deposition (N_C, mmol g^{-1}) in the methane conversion stage is calculated by the carbon balance.

$$N_C = N_{CH_4,in} - N_{CH_4,out} - N_{CO} - N_{CO_2} \tag{E7}$$

In the water splitting stage, the H$_2$ was generated from both the oxidation of oxygen carrier (R4) and the carbon gasification reactions ((R6) and (R2)). The yield of H$_2$ from the carbon gasification ($N_{H2,GC}$,

Table 1
the lattice parameters of the fresh perovskites.

Samples	Lattice structure	Space group	Crystal size (nm)	a (Å)	b (Å)	c (Å)	Vol (Å^3)
LaMnO$_{3+\delta}$	Hexagonal	R-3c	52.2	5.518	5.518	13.355	352.21
LaMn$_{0.9}$Co$_{0.1}$O$_{3+\delta}$	Hexagonal	R-3c	58.5	5.521	5.521	13.354	352.51
LaMn$_{0.7}$Co$_{0.3}$O$_{3+\delta}$	Orthorhombic	Pbnm	57.2	5.526	5.479	7.772	235.31
LaMn$_{0.5}$Co$_{0.5}$O$_{3+\delta}$	Orthorhombic	Pbnm	55.0	5.523	5.484	7.774	235.46
La$_{0.8}$Sr$_{0.2}$Mn$_{0.5}$Co$_{0.5}$O$_{3+\delta}$	Orthorhombic	Pbnm	34.1	5.523	5.480	7.786	235.64
La$_{0.6}$Sr$_{0.4}$Mn$_{0.5}$Co$_{0.5}$O$_{3+\delta}$	Orthorhombic	Pbnm	30.1	5.523	5.476	7.785	235.47

Fig. 3. XPS spectra for O 1s(a), Mn2p (b) and Co2p (c) of fresh LaMnO$_{3+\delta}$(A), LaMn$_{0.9}$Co$_{0.1}$O$_{3+\delta}$(B), LaMn$_{0.7}$Co$_{0.3}$O$_{3+\delta}$(C), LaMn$_{0.5}$Co$_{0.5}$O$_{3+\delta}$(D), La$_{0.8}$Sr$_{0.2}$Mn$_{0.5}$Co$_{0.5}$O$_{3+\delta}$(E), La$_{0.6}$Sr$_{0.4}$Mn$_{0.5}$Co$_{0.5}$O$_{3+\delta}$(F).

mmol g^{-1}) and the oxidation of oxygen carriers ($N_{H2,OOC}$, mmol g^{-1}) are:

$$N_{H_2,GC} = N_{CO} + 2N_{CO_2} \tag{E8}$$

$$N_{H_2,OOC} = N_{H_2}\text{-}N_{H_2,GC} \tag{E9}$$

the available oxygen capacity (ω, wt%) is:

$$\omega = 0.016(2N_{CO_2} + N_{CO} + 2(N_{CH_4,in} - N_{CH_4,out}) - N_{H_2})/m \times 100\% \tag{E10}$$

3. Results and discussion

3.1. Characterization of La$_{1-x}$Sr$_x$Mn$_{1-y}$Co$_y$O$_{3+\delta}$ oxygen carriers

The phase, crystal structure, lattice parameters and crystal size of the La$_{1-x}$Sr$_x$Mn$_{1-y}$Co$_y$O$_{3+\delta}$ perovskites were investigated by XRD and the results are illustrated in Fig. 2 and Table 1. The patterns of LaMnO$_{3+\delta}$ sample matched well with LaMnO$_{3.15}$ perovskite (JCPDS #50-0298), which is corresponding to the structure of hexagonal and space group of R-3c [23]. The peaks with 2θ of 32°, 40°, 52°, 58°, 68° and 78° split into twin peaks in the diffraction patterns (the peaks around 32° is shown in Fig. 2(b)). This
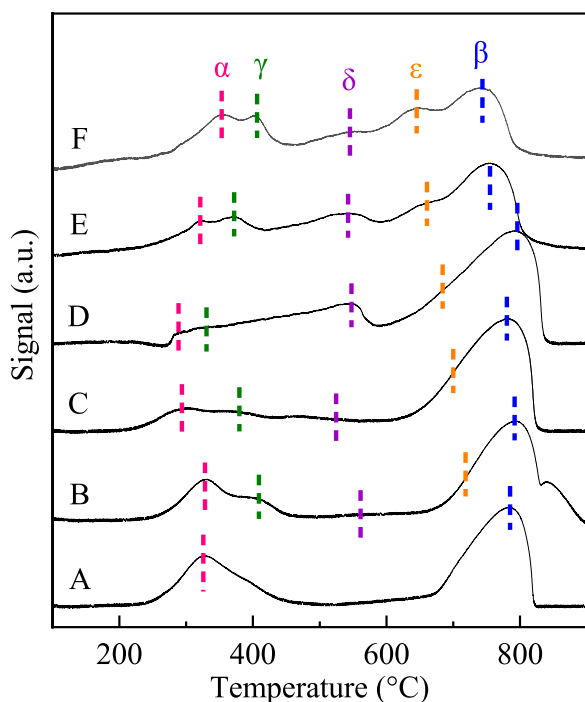
Table 2
Molar percentage of surface element for the fresh perovskites measured by XPS.

Samples	Mn $2p_{3/2}$		Co $2p_{3/2}$		O 1s		
	Mn^{3+}	Mn^{4+}	Co^{2+}	Co^{3+}	OI	OII	OIII
$LaMnO_{3+\delta}$	57.71	42.29	-	-	48.13	45.93	5.94
$LaMn_{0.9}Co_{0.1}O_{3+\delta}$	57.23	42.77	52.42	47.58	50.04	44.55	5.41
$LaMn_{0.7}Co_{0.3}O_{3+\delta}$	57.37	42.63	47.66	52.34	52.14	40.92	6.94
$LaMn_{0.5}Co_{0.5}O_{3+\delta}$	56.12	43.88	42.74	57.26	60.95	31.39	7.66
$La_{0.8}Sr_{0.2}Mn_{0.5}Co_{0.5}O_{3+\delta}$	55.08	44.92	41.43	58.57	55.18	38.70	6.12
$La_{0.6}Sr_{0.4}Mn_{0.5}Co_{0.5}O_{3+\delta}$	54.66	45.34	40.35	59.65	54.37	41.33	4.30

confirms the lattice distortion from the ideal cubic symmetry originating from the Jahn-Teller effect attributed to the interaction between Mn^{3+} cation and a weak field ligand O^{2-} as well as the change of ionic radii [24]. The pattern of $LaMn_{0.9}Co_{0.1}O_{3+\delta}$ sample highly coincided with that of $LaMnO_{3+\delta}$, which indicates hexagonal structure and R-3c space group. For the $LaMn_{0.7}Co_{0.3}O_{3+\delta}$, $LaMn_{0.5}Co_{0.5}O_{3+\delta}$, $La_{0.8}Sr_{0.2}Mn_{0.5}Co_{0.5}O_{3+\delta}$ and $La_{0.6}Sr_{0.4}Mn_{0.5}Co_{0.5}O_{3+\delta}$ perovskites, the twin peaks coalesced into single peaks in the patterns, suggesting that the lattice tends to a higher symmetry as the amount of Co substitution increased [24,25]. These diffraction patterns were in good agreement with $LaMnO_{3.11}$ (#50–0297), which suggests orthorhombic structure of these perovskites [26–30]. Fig. 2 also shows that single perovskite phases were generated for the $LaMn_{1-y}Co_yO_{3+\delta}$ oxygen carriers and no additional peaks on account of impurities were found. This indicates that all the Co incorporate into the perovskite lattice completely. In the patterns of $La_{0.8}Sr_{0.2}Mn_{0.5}Co_{0.5}O_{3+\delta}$ and $La_{0.6}Sr_{0.4}Mn_{0.5}Co_{0.5}O_{3+\delta}$ samples, weak peaks for Ruddlesden-Popper (R-P) perovskite [15,31] $La_{0.4}Sr_{1.6}MnO_4$ (#51–0116) and perovskite $SrCoO_3$ (#38–1148) were detected and the peak intensity increased with the Sr content, since the Sr cations did not completely incorporate into the $LaMn_{1-y}Co_yO_{3+\delta}$ structure but leaded to the formation of other perovskites. Table 1 shows that the crystal size of $LaMn_{0.9}Co_{0.1}O_{3+\delta}$, $LaMn_{0.7}Co_{0.3}O_{3+\delta}$ and $LaMn_{0.5}Co_{0.5}O_{3+\delta}$ were larger than $LaMnO_{3+\delta}$, which indicates that the cobalt substitution increases the crystallinity of perovskite oxide. On the contrary, the crystal size of $La_{0.8}Sr_{0.2}Mn_{0.5}Co_{0.5}O_{3+\delta}$ and $La_{0.6}Sr_{0.4}Mn_{0.5}Co_{0.5}O_{3+\delta}$ was smaller

than that of $LaMn_{0.5}Co_{0.5}O_{3+\delta}$, since the doping of Sr might block the crystal growth [17,32]. This could be confirmed by the larger peak width as shown in Fig. 2(b). The lattice volume of $LaMn_{0.9}Co_{0.1}O_{3+\delta}$ was slightly larger than that of $LaMnO_{3+\delta}$ and that of $LaMn_{0.5}Co_{0.5}O_{3+\delta}$ was slightly larger than $LaMn_{0.7}Co_{0.3}O_{3+\delta}$, which can be ascribed to the fact that the average ionic radius of Co^{2+}(0.745 Å) and Co^{3+}(0.61 Å) is larger than that of Mn^{3+} (0.645 Å) and Mn^{4+} (0.53 Å). The substitution of Mn cations by larger Co cations leads to lattice expansion. The lattice volume was approximate for the three $La_{1-x}Sr_xMn_{0.5}Co_{0.5}O_{3+\delta}$ perovskites (x=0, 0.2 and 0.4). The substitution of La^{3+} (1.36 Å) by larger Sr^{2+} (1.44 Å) cations increases the lattice volume. However, the substitution of La^{3+} by Sr^{2+} caused the conversion of Mn^{3+} to Mn^{4+} and Co^{2+} to Co^{3+} to preserve the electroneutrality of the perovskite crystal. The Mn^{4+} and Co^{3+} with smaller ionic radius result in the lattice shrinkage. The effect of Sr substitution on lattice volume synthesized these two factors.

The surface properties of each perovskite were investigated by XPS and the analysis of the results is shown in Fig. 3 and Table 2. According to Fig. 3 (a), the spectra of Mn $2p_{3/2}$ and Mn $2p_{1/2}$ for each perovskite were respectively fitted into two peaks corresponding to Mn^{3+} (642.1 eV and 653.5 eV) and Mn^{4+} (644.4 eV and 655.8 eV) [9,33]. The exist of Mn^{4+} leads to the nonstoichiometric excess oxygen in the $LaMnO_{3+\delta}$-based perovskites. The formation of Mn^{4+} and the oxygen stoichiometric depends on the preparation condition: annealing in absence of oxygen generates few Mn^{4+} and results in stoichiometric $LaMnO_3$, while the nonstoichiometric $LaMnO_{3+\delta}$ with a considerable amount of Mn^{4+} could be calcinated in air. $LaMnO_{3+\delta}$ is the only lanthanum-transition-metal perovskite (first row transition metal) with nonstoichiometric excess oxygen [34]. As shown in Table 2, the molar proportion of Mn^{4+} in the $LaMn_{1-y}Co_yO_{3+\delta}$ perovskites increased gradually with the Co content. This could be attributed to that the Co cations incorporating into perovskite lattice contain a considerable amount of Co^{2+}, this Co^{2+} can convert some Mn^{3+} into Mn^{4+} to compensate for the decrease of positive charge. The introduction of Sr also leaded to the augment of molar proportion of Mn^{4+}, since the substitution of La^{3+} by Sr^{2+} also causes the generation of additional Mn^{4+} to maintain electroneutrality of the perovskite crystal. Fig. 3(b) presents the spectra of the Co 2p of each perovskite. The spectra of Co 2p were fitted with four peaks accompanying with two satellite peaks. The peaks at binging energy of 779.6–780.0 eV and 795.4 eV were assigned to Co^{3+}, the peaks at 781.0–781.5 eV and 796.8 eV were ascribed to Co^{2+}, and the satellite peaks were corresponding to the binging energy of 784.9–791.0 eV [35]. The binding energy of the peaks of Co $2p_{3/2}$ for the three $La_{1-x}Sr_xMn_{0.5}Co_{0.5}O_{3+\delta}$ perovskites was higher than that for $LaMn_{0.9}Co_{0.1}O_{3+\delta}$ and $LaMn_{0.7}Co_{0.3}O_{3+\delta}$. This leads to a greater distance between the both peaks of Co $2p_{3/2}$ and Co $2p_{1/2}$ at the low proportion of Co doping, which suggests high proportion of Co^{2+} when the Co content is low [35]. It can be observed from Table 2 that the molar proportion of Co^{3+} rose and that of Co^{2+} declined as the Co content increased for the $LaMn_{1-y}Co_yO_{3+\delta}$ oxygen carriers. This deduces that both Mn and Co cations on the surface of perovskite particles are favored to higher oxidation states with the increasing Co content. For the three $La_{1-x}Sr_xMn_{0.5}Co_{0.5}O_{3+\delta}$ perovskites (x=0, 0.2 and 0.4), more Co^{3+} was generated with the Sr-doping amount, due to the conversion of some Co^{2+} into Co^{3+} to compensate the decrease of positive charge resulting from the substitution of La^{3+} by Sr^{2+}. The XPS signals of the O1s are shown in Fig. 3(c). As can be seen, the spectra

Fig. 4. H_2-TPR profiles of fresh $LaMnO_{3+\delta}$(A), $LaMn_{0.9}Co_{0.1}O_{3+\delta}$(B), $LaMn_{0.7}Co_{0.3}O_{3+\delta}$(C), $LaMn_{0.5}Co_{0.5}O_{3+\delta}$(D), $La_{0.8}Sr_{0.2}Mn_{0.5}Co_{0.5}O_{3+\delta}$(E), $La_{0.6}Sr_{0.4}Mn_{0.5}Co_{0.5}O_{3+\delta}$(F).

Table 3

The amount of oxygen release (H$_2$ consumption) during the reduction process for each fresh oxygen carrier measured by H$_2$-TPR (mmol g^{-1}).

Samples	Peak α	Peak γ	Peak δ	Peak ε	Peak β	Total
LaMnO$_{3+\delta}$	0.89	0.00	0.00	0.00	1.64	2.54
LaMn$_{0.9}$Co$_{0.1}$O$_{3+\delta}$	0.55	0.21	0.08	0.28	1.60	2.74
LaMn$_{0.7}$Co$_{0.3}$O$_{3+\delta}$	0.32	0.38	0.28	0.65	1.29	2.91
LaMn$_{0.5}$Co$_{0.5}$O$_{3+\delta}$	0.19	0.40	0.41	0.84	1.31	3.15
La$_{0.8}$Sr$_{0.2}$Mn$_{0.5}$Co$_{0.5}$O$_{3+\delta}$	0.33	0.44	0.45	0.78	1.21	3.22
La$_{0.6}$Sr$_{0.4}$Mn$_{0.5}$Co$_{0.5}$O$_{3+\delta}$	0.51	0.48	0.40	0.88	0.97	3.24

of oxygen can be fitted into three peaks arising from the lattice oxygen (OI), the surface chemisorbed oxygen (OII) and the physical adsorbed oxygen (OIII). The lattice oxygen possessed the lowest binding energy around 529.4 eV. The surface chemisorbed oxygen includes the carbonates and hydroxyl species and its binding energy was about 531.4 eV. The physical adsorbed oxygen such as adsorbed water could be assigned to the binding energy of 533.3 eV [24,36,37]. The binding energy of the chemisorbed oxygen (OII) for the three La$_{1-x}$Sr$_x$Mn$_{0.5}$Co$_{0.5}$O$_{3+\delta}$ perovskites decreased compared with the LaMn$_{1-y}$Co$_y$O$_{3+\delta}$ perovskites (y=0, 0.1, 0.3), which means that the activity of the chemisorbed oxygen is enhanced for the La$_{1-x}$Sr$_x$Mn$_{0.5}$Co$_{0.5}$O$_{3+\delta}$ perovskites. According to Table 2, the percentage of the lattice oxygen for LaMn$_{1-y}$Co$_y$O$_{3+\delta}$ perovskites increased while the chemisorbed oxygen declined with the cobalt-doping amount. It can be seen from comparison of the three La$_{1-x}$Sr$_x$Mn$_{0.5}$Co$_{0.5}$O$_{3+\delta}$ perovskites
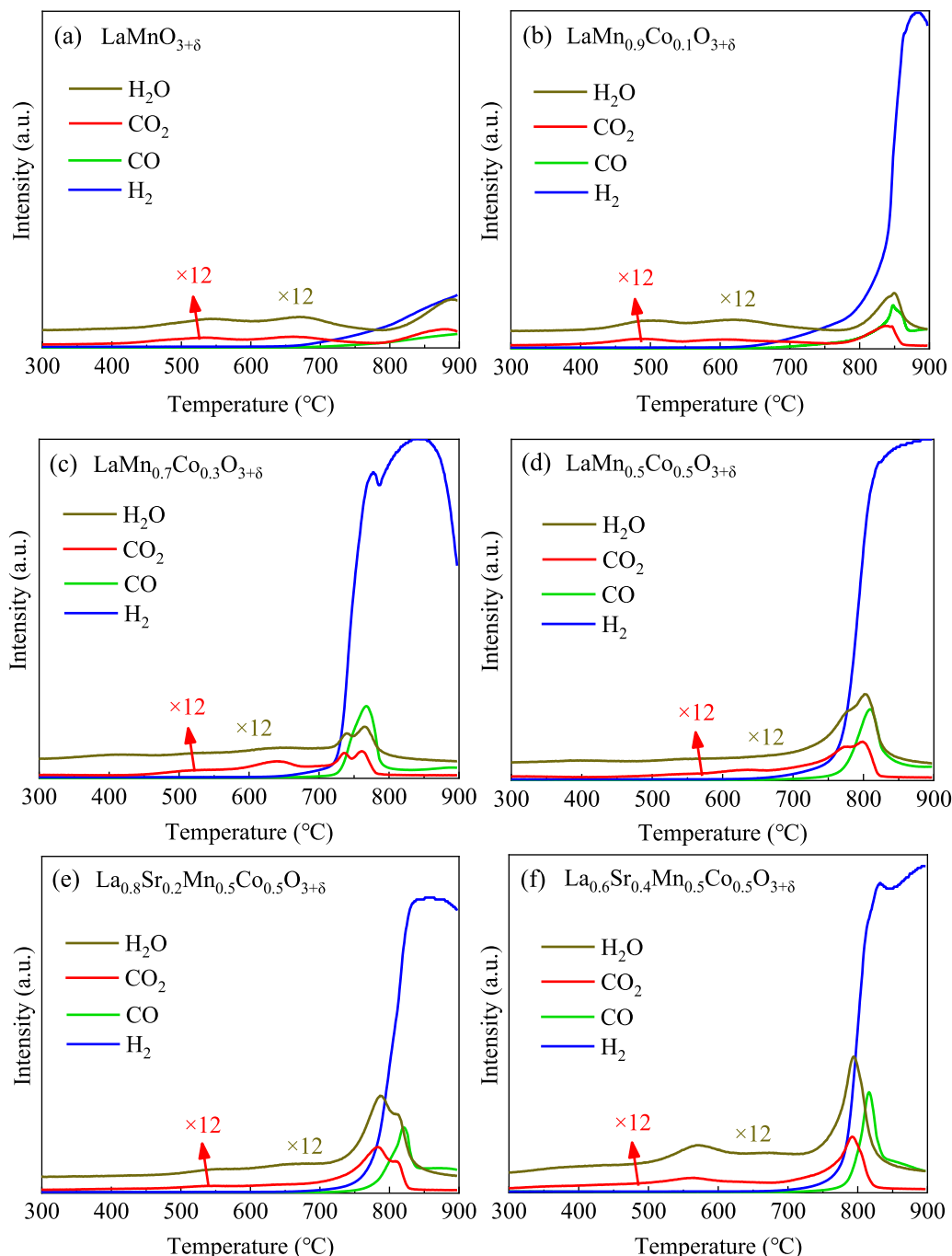
Fig. 5. CH$_4$-TPR profiles of each fresh perovskite oxygen carrier.
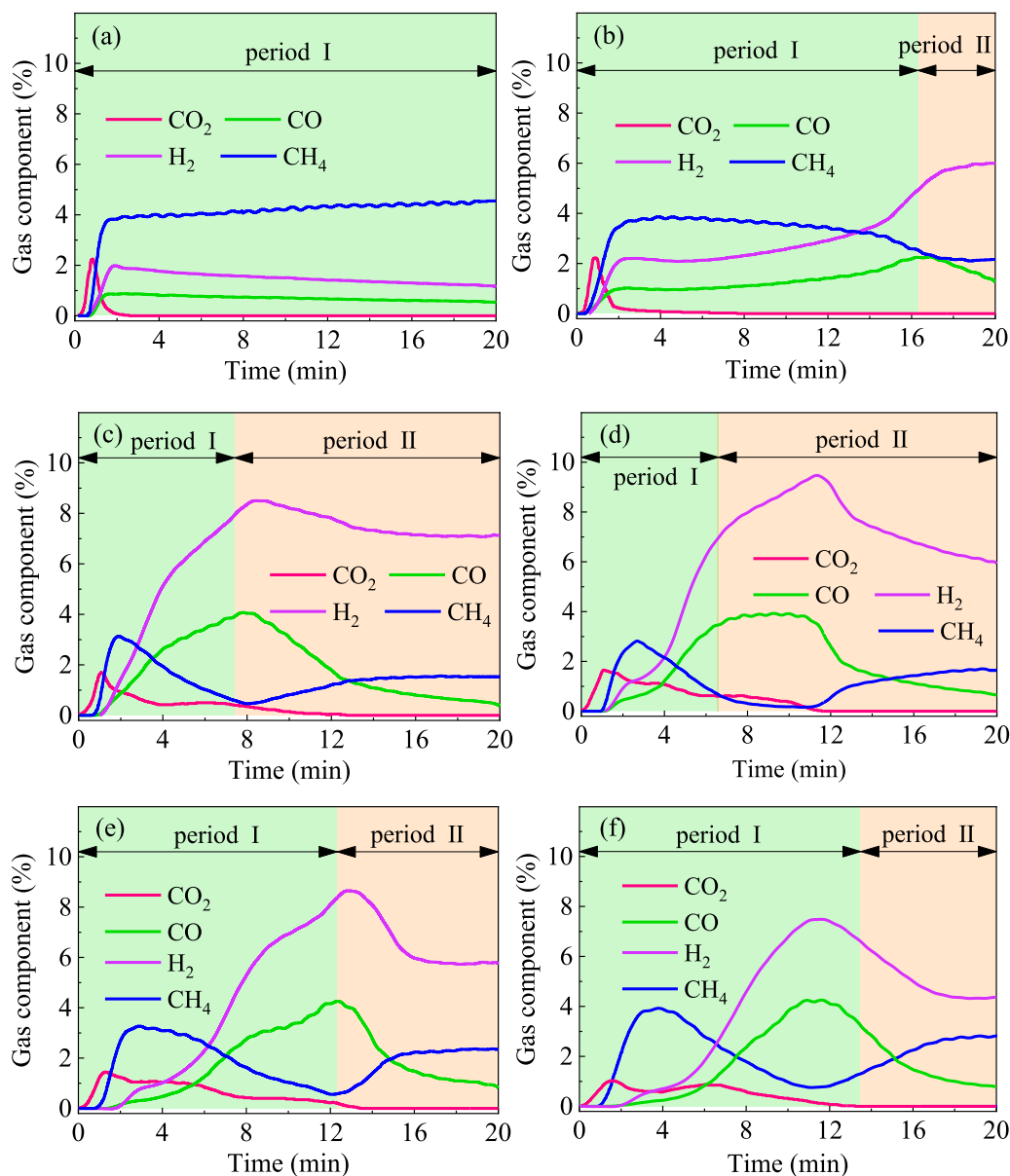
Fig. 6. The component of the outlet gas for $LaMnO_{3+\delta}$(a), $LaMn_{0.9}Co_{0.1}O_{3+\delta}$(b), $LaMn_{0.7}Co_{0.3}O_{3+\delta}$(c), $LaMn_{0.5}Co_{0.5}O_{3+\delta}$(d), $La_{0.8}Sr_{0.2}Mn_{0.5}Co_{0.5}O_{3+\delta}$(e), and $La_{0.6}Sr_{0.4}Mn_{0.5}Co_{0.5}O_{3+\delta}$(f) in the methane conversion stage at 850 °C. period I: methane reforming period, period II: carbon deposition period.

that the proportion of the lattice oxygen decreased while the chemisorbed oxygen rose with the Sr-doping amount. The substitution of La^{3+} by Sr^{2+} promotes the addition of oxygen vacancies to compensate for the decrease of positive charge of the perovskite crystal (Fig. S3). The oxygen vacancies may be the adsorption sites for oxygen and the introduction of Sr increases the amount of the chemisorbed oxygen.

H$_2$-TPR measurement was carried out to explore the effect of Co and Sr doping on the reducibility of each perovskite, as present in Fig. 4. It can be seen that the H$_2$-TPR profiles of the perovskites exhibited five peaks labeled as α, β, γ, δ and ε, respectively. The peaks α ranging from 240 to 450 °C were attributed to the reduction of Mn^{4+} into Mn^{3+} [9, 30]. The peaks β appearing at the temperature higher than 700 °C were associated with the further reduction of Mn^{3+} into Mn^{2+} [38]. The perovskite structure could destruct in this reduction process [29,30]. For the cobalt-doping perovskites, the peaks γ forming in range of 350–500 °C may originate from the reduction of surface Co^{3+} into Co^{2+} [29]. The peaks δ ranging from 500 to 600 °C could be ascribed to the reduction of bulk Co^{3+} into Co^{2+}, and the peaks ε present in 600–750 °C could be on account of the reduction of Co^{2+} into Co^0. For

the $LaMn_{1-y}Co_yO_{3+\delta}$ oxygen carriers, the temperature of peaks α and γ declined with the Co-substitution proportion, indicating that the introduction of Co enhances the activity of the oxygen combining with Mn^{4+} and surface Co^{3+}. The temperature of peaks ε also decreased as the Co content increased. This arises from that oxygen vacancies are generated after the Mn^{4+} are reduced into Mn^{3+} (in this case, the non-stoichiometric excess oxygen is exhausted, and the $LaMn_{1-y}Co_yO_{3+\delta}$ transforms into $LaMn_{1-y}Co_yO_{3-\delta}$). The introduction of Co could cause the increase of oxygen vacancies which accelerates the migration of oxygen anion, decreasing the temperature of peaks ε [4,15,39]. The temperature of peaks β was approximately constant with Co content, which suggests the Co substitution has little effect on the reduction of Mn^{3+} into Mn^{2+}. Table 3 presents the amount of the oxygen released during each reduction peak and the whole process for each oxygen carrier in the H$_2$-TPR detection. It can be observed that the area of peaks α and peaks β decreased with the proportion of Co substitution, resulting from the decrease of the real amount of Mn cations as mentioned above. On the contrary, the area of peaks γ, δ and ε gradually enlarged with Co-doping proportion due to the increase of Co content. The total amount of oxygen

released during the whole H_2-TPR process increased with the Co content, indicating higher oxygen storage capability (OSC) at more Co doping amount. This originates from that more lattice oxygen can be release from the reduction process of Co^{3+}/Co^{2+} into Co^0 than Mn^{4+}/Mn^{3+} into Mn^{2+}. For the three $La_{1-x}Sr_xMn_{0.5}Co_{0.5}O_{3+\delta}$ oxygen carriers, the temperature of peaks α and γ increased with the Sr content, suggesting that the incorporation of Sr into perovskite lattice might block the reduction of Mn^{4+} and Co^{3+}. The temperature of peaks ε and β decreased with the Sr-doping proportion. This is attributed to that the oxygen vacancies arising from the substitution of La^{3+} by Sr^{2+} promote the conduction of oxygen anion. It can be seen in Table 3 that the area of peaks α and γ increased with Sr-substitution proportion, consistent with the increase of Mn^{4+} and Co^{3+} as shown in Table 2. The area of peaks β declined with the Sr content, indicating that the introduction of Sr might lead to the decrease of the reduction degree of Mn^{3+}. The total amount of the released oxygen rose with the Sr-doping proportion, attributed to that the Sr substitution increases the amount of Mn^{4+} and Co^{3+} (Table 2), which means that the doping of Sr could enhance the OSC of these perovskite oxygen carriers.

CH4-TPR was performed to further investigate the reactivity of deep oxidation (complete oxidation) and selective oxidation (partial oxidation) of methane for the perovskite oxygen carriers, and the results are displayed in Fig. 5. Deep oxidation is capable of oxidizing CH_4 to H_2O and CO_2 by the unselective oxygen species with high activity. Selective oxidation converts methane into syngas by the selective and low active oxygen species (bulk lattice oxygen). For $LaMnO_{3+\delta}$ oxygen carrier as shown in Fig. 5(a), deep oxidation mainly occurred to oxidize methane into CO_2 and H_2O at the temperature ranging of 450–750 °C. The unselective oxygen specie is probably surface absorbed oxygen and the most of the oxygen released from the reduction of Mn^{4+} into Mn^{3+}. When the temperature rose above 700, methane was primarily selectively oxidized into CO and H_2 by the selective oxygen specie which may be the majority of oxygen released in the reduction process of Mn^{3+} into Mn^{2+}[9]. As can be observed in Fig. 5(b)–(d), another peak of CO_2 and H_2O appeared at the temperature from 700 to 850 for the $LaMn_{1-y}Co_yO_{3+\delta}$ perovskites, and the area of the peak enlarged with the proportion of Co substitution. This peak is likely to be ascribed to the reduction of Co^{3+} into Co^{2+}, and the increase of the Co^{3+} (Table 2) leads to the enlargement of this peak. The peak area of CO of $LaMn_{1-y}Co_yO_{3+\delta}$ perovskites was larger than that of $LaMnO_{3+\delta}$, and it increased with the Co content. This peak might be on account of the reduction of both Mn^{3+} into Mn^{2+} and Co^{2+} into Co^0, and the enlargement of this peak originates from that more lattice oxygen can be release from the reduction process of Co^{2+} into Co^0 than Mn^{3+} into Mn^{2+}. For three $La_{1-x}Sr_xMn_{0.5}Co_{0.5}O_{3+\delta}$ oxygen carriers, it can be seen from the comparation of Fig. 5(d)–(f) that the peak intensity of CO_2 and H_2O at the temperature above 700 increased with the Sr-doping amount, which is attributed to the increase of the Co^{3+} caused by the substitution of Sr^{2+} (Table 2). The peak intensity of CO_2 and H_2O appeared at the temperature about 565 was obviously heightened, probably resulting from the increase of Mn^{4+} and surface observed oxygen (Table 2). In addition, it is obvious in Fig. 5(b)–(f) that the intensity of peak H_2 was higher than twice the peak of CO for each Co doped perovskite, indicating occurrence of methane cracking reaction (R5) and formation of carbon deposition. The intensity of peak H_2 for $La_{1-x}Sr_xMn_{0.5}Co_{0.5}O_{3+\delta}$ in Fig. 5 (e) and (f) was lower than that for $LaMn_{1-y}Co_yO_{3+\delta}$ perovskites, which means that Sr doping exhibits resistance towards carbon deposition.

3.2. Redox performance of $La_{1-x}Sr_xMn_{1-y}Co_yO_{3+\delta}$ oxygen carriers

The performance of $La_{1-x}Sr_xMn_{1-y}Co_yO_{3+\delta}$ perovskites for CLSMR was investigated in the fixed-bed reactor at 850 °C, and the various properties are presented in Figs. 6–9, Fig. S1–S2 and Fig. S4–S6.

The component of the outlet gas for the perovskites in the methane conversion stage is depicted in Fig. 6. According to Fig. 6(a)–(f), the component of CO_2 of all perovskites increased sharply to a maximum value in the initial. This results from a deep oxidation of methane. Afterward, the
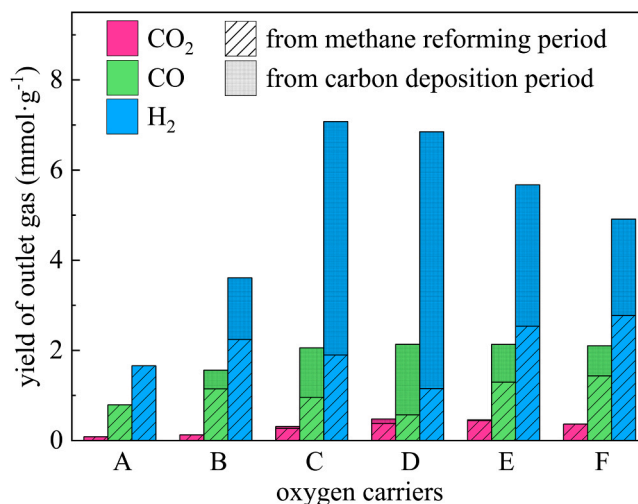

Fig. 7. The yield of the produced gas of $LaMnO_{3+\delta}$(A), $LaMn_{0.9}Co_{0.1}O_{3+\delta}$(B), $LaMn_{0.7}Co_{0.3}O_{3+\delta}$(C), $LaMn_{0.5}Co_{0.5}O_{3+\delta}$(D), $La_{0.8}Sr_{0.2}Mn_{0.5}Co_{0.5}O_{3+\delta}$(E), and $La_{0.6}Sr_{0.4}Mn_{0.5}Co_{0.5}O_{3+\delta}$(F) in the methane conversion stage at 850 °C.

component of CO_2 declined to zero while that of CO and H_2 rosed, which indicates that the selective oxidation was dominant. The deep oxidation and selective oxidation are mentioned in the Section 3.1. For the $LaMn_{1-y}Co_yO_{3+\delta}$ perovskites as illustrated in Fig. 6(a)–(d), the maximum value of the CO_2 generation rate decreased as the proportion of Co substitution increased. This is attributed to that the CO_2 is generated from the deep oxidation of methane by Mn^{4+} in the initial. The Co doping decreased the real amount of Mn^{4+}, leading to the decrease of the initial generation rate of CO_2. Thereafter, the CO_2 generation rate declined more slowly with the Co content, resulting from that the CO_2 is produced from the reduction of part Co^{3+} to Co^{2+} at this time and the increase of Co^{3+}(Table 2) gives rise to a higher generation rate of CO_2. These are consistent with the decrease of the area of peaks α and the increase of the area of peaks γ in the H_2-TPR results (Fig. 4). The component of CO and H_2 increased with the Co substitution amount, which means that the Co doping could enhance the release rate of selective oxygen. This would be discussed in detail in the 3.5 section. It can be observed from Fig. 6(d)–(f) that the component of CO_2 for the three $La_{1-x}Sr_xMn_{0.5}Co_{0.5}O_{3+\delta}$ oxygen carriers decreased on the whole, since the Sr cations may restrain the absorption and activation of methane molecules. The maximum of the CO component of $La_{0.8}Sr_{0.2}Mn_{0.5}Co_{0.5}O_{3+\delta}$ and $La_{0.6}Sr_{0.4}Mn_{0.5}Co_{0.5}O_{3+\delta}$ was higher than that of $LaMn_{0.5}Co_{0.5}O_{3+\delta}$, and the maximum of the CO component of $La_{0.6}Sr_{0.4}Mn_{0.5}Co_{0.5}O_{3+\delta}$ appeared earlier than $LaMn_{0.5}Co_{0.5}O_{3+\delta}$ and $La_{0.8}Sr_{0.2}Mn_{0.5}Co_{0.5}O_{3+\delta}$. This indicates that the migration of oxygen anion and the release of selective oxygen are promoted by the increase of oxygen vacancies (Fig. S3), which is consistent with the decrease of the temperature of peak β and ε (Fig. 4). The component of the unreacted methane increased slightly with the Sr content during the whole reduction stage, suggesting less consumption of methane at a higher proportion of Sr doping. This may be attributed to that the Sr cations inhibit the adsorption or activation of the methane molecules.

For all the oxygen carriers except $LaMnO_{3+\delta}$, the component of CO rosed to a maximum and then declined while that of H_2 maintained constant approximately or declined relatively slowly in late period of the methane conversion stage, leading to the molar ratio of H_2/CO greater than 2. This is account of carbon formation from methane cracking reaction (R5). In view of whether carbon deposition occurs, the process of the methane conversion stage of each perovskite could be demarcated into two periods: methane reforming period and carbon deposition period. The former is the early period of the reduction stage without carbon formation and the H_2/CO during this period is slightly less than 2 or equal to 2. The carbon deposition period located in the late period of the reduction stage with the H_2/CO is greater than 2. It can be observed in Fig. 6(a)–(f) that the introduction of Co caused the carbon formation
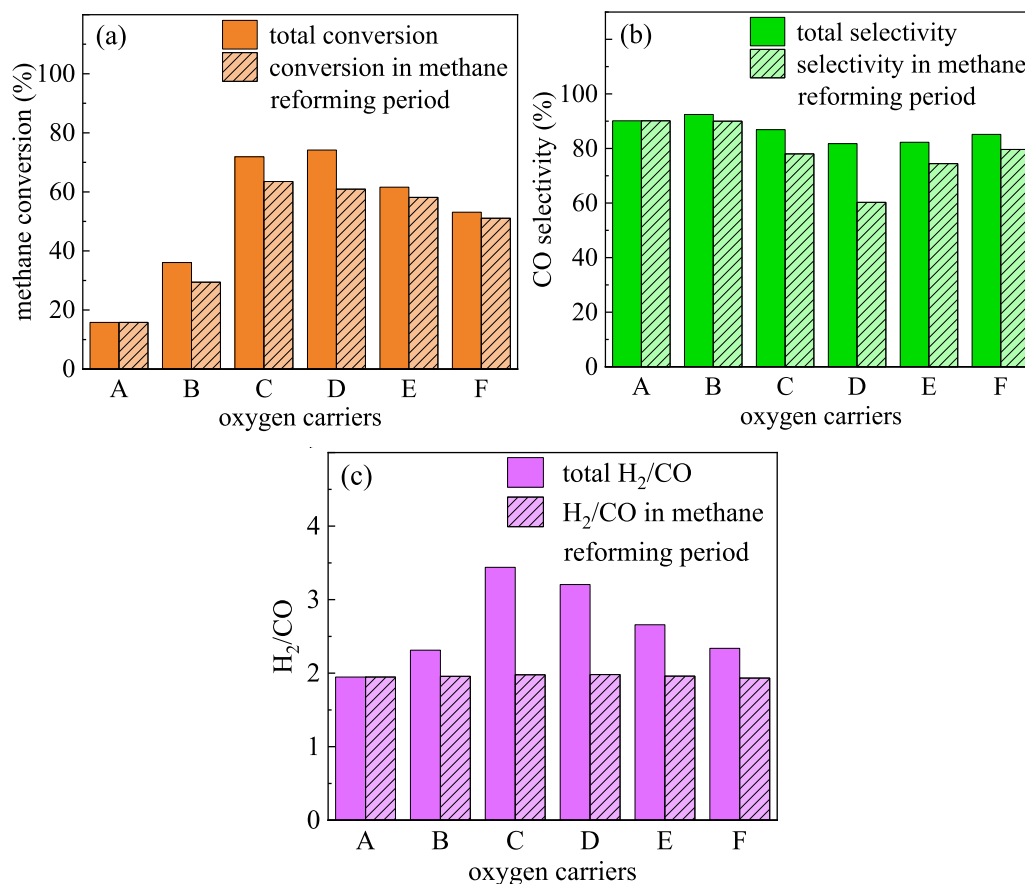
Fig. 8. The methane conversion(a), the CO selectivity(b) and the molar ratio of H_2/CO(c) of $LaMnO_{3+\delta}$(A), $LaMn_{0.9}Co_{0.1}O_{3+\delta}$(B), $LaMn_{0.7}Co_{0.3}O_{3+\delta}$(C), $LaMn_{0.5}Co_{0.5}O_{3+\delta}$(D), $La_{0.8}Sr_{0.2}Mn_{0.5}Co_{0.5}O_{3+\delta}$(E), and $La_{0.6}Sr_{0.4}Mn_{0.5}Co_{0.5}O_{3+\delta}$(F) in the methane conversion stage at 850 °C.

to occur earlier, shortening the duration of the methane reforming period, while the doping of Sr can delay the occurrence of carbon deposition, causing a longer methane reforming period.

The yield of the produced gas of the perovskites in the methane conversion stage is illustrated in Fig. 7. It can be observed that the total yield of CO_2 for the $LaMn_{1-y}Co_yO_{3+\delta}$ perovskites increased with the cobalt-doping amount, since both Mn and Co cations are favored to higher oxidation states with the increasing cobalt substitution proportion (Table 2). The total yield of CO of the $LaMn_{1-y}Co_yO_{3+\delta}$ perovskites also increased with the Co content, arising from that more selective oxygen can be released from the reduction process of Co^{2+} into Co^0 than Mn^{3+} into Mn^{2+}. The total H_2 yield rose on the whole as the Co-substitution proportion increased, resulting from that Co promotes methane cracking reaction to generate superfluous hydrogen. For the three $La_{1-x}Sr_xMn_{0.5}Co_{0.5}O_{3+\delta}$ perovskites, the yield of CO_2 and CO both decreased slightly as the Sr-doping proportion increased. This may be ascribed to the inhibition of the absorption and activation of methane. The H_2 yield declined with the Sr substitution amount due to the resistance towards carbon deposition of Sr doping.

Carbon deposition is a negative factor and leads to many harmful effects in the CLSMR process as mentioned in the introduction section. Thus, the carbon deposition period should be avoided. Only the syngas produced in the methane reforming period is effective and usable. Fig. 7 also presents the yield of each gas generated in the methane reforming period and carbon deposition period. It can be observed that the proportion of the yield for each gas produced in the methane reforming period to the total yield decreased with the Co content for the $LaMn_{1-y}Co_yO_{3+\delta}$ perovskites, and increased with the Sr-doping amount for the $La_{1-x}Sr_xMn_{0.5}Co_{0.5}O_{3+\delta}$ perovskites. This is attributed to the variation of the duration of the methane reforming period shown in Fig. 6. It can be

deduced that the doping of Co decreases the yield of the effective syngas while this yield can be raised by the introduction of Sr.

Fig. 8 depicts the methane conversion, the CO selectivity and the molar ratio of H_2/CO of the perovskite oxygen carriers in the methane conversion stage. According to Fig. 8(a), the total CH_4 conversion increased with the cobalt-substitution proportion, but decreased with the strontium content, which means that the cobalt doping can enhance the reactivity of perovskites, while the Sr substitution causes the perovskite less reactive. This results from that the introduction of Co enhances the complete oxidation, partial oxidation and methane decomposition, increasing the consumption of methane, while the doping of Sr has the opposite effect, as shown in Figs. 6 and 7. The detailed mechanisms that cause these phenomena have been described above. The CH_4 conversion in the methane reforming period was lower than the total conversion since the consumption of methane in the carbon deposition period was greater than that in the methane reforming period. The effect of Co and Sr doping on the CH_4 conversion in reforming period is the same as that of total methane conversion, and the reason is the same. Fig. 8(b) shows that total CO selectivity decreased with the Co-doping amount on the whole, while it rose with the Sr content. This is ascribed to that the yield of CO_2 is enhanced by the cobalt doping and lessened by the Sr doping (Fig. 7). Although the CO yield exhibits the same variation trend, the CO_2 yield has a more significant effect on the CO selectivity than CO. The CO selectivity in the methane reforming period was lower than the total CO selectivity, since a considerable amount of CO is produced in the carbon deposition stage, and no or very little CO_2 is produced. The variation trend of CO selectivity with the amount of Co and Sr in methane reforming stage was the same as that of total CO selectivity for the same reasons. Fig. 8(c) depicts that the total H_2/CO increased with the Co doping amount, while
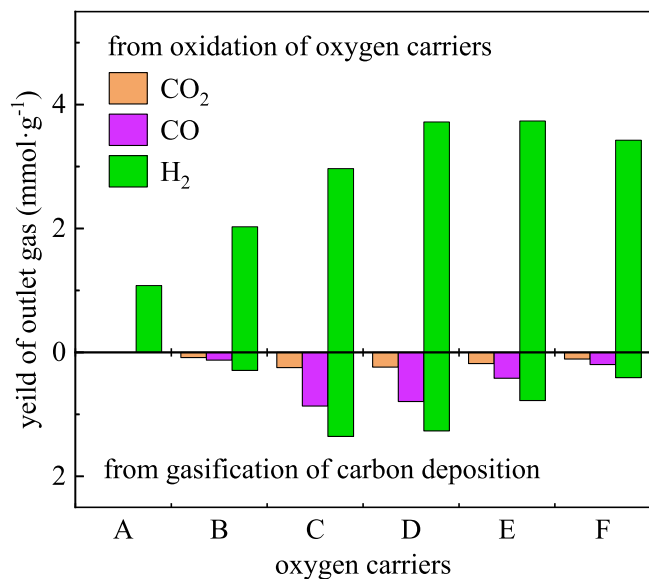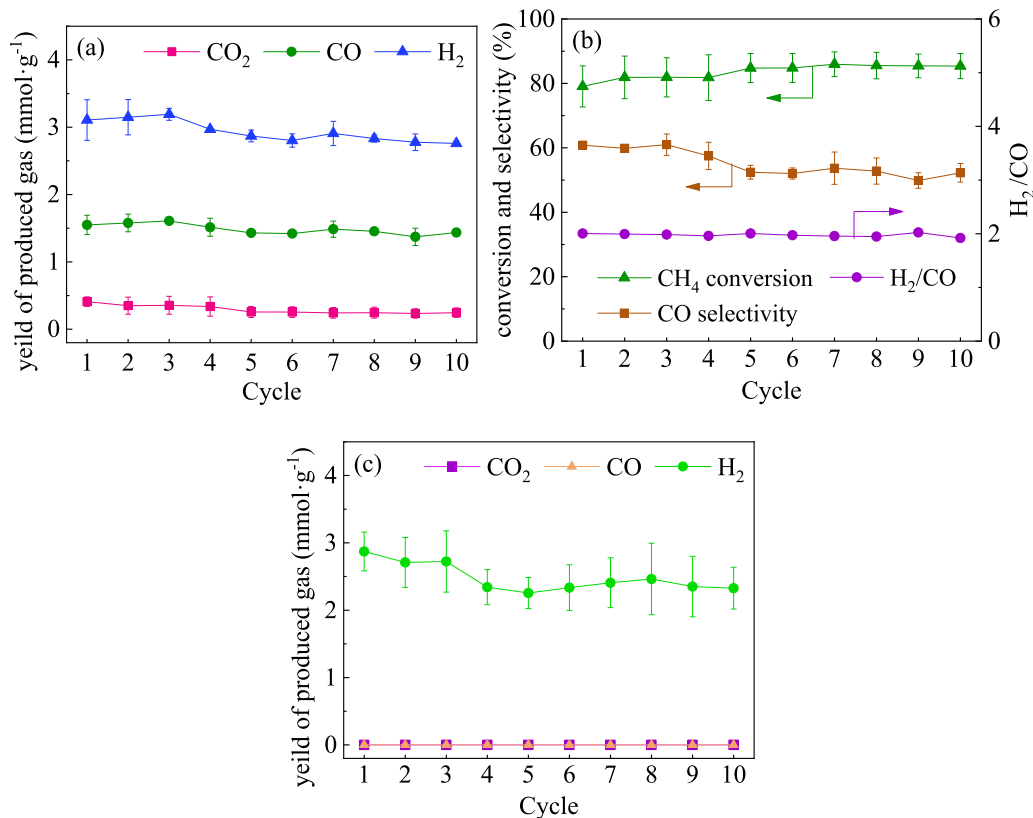
Fig. 9. The yield of the produced gas of $LaMnO_{3+\delta}$(A), $LaMn_{0.9}Co_{0.1}O_{3+\delta}$(B), $LaMn_{0.7}Co_{0.3}O_{3+\delta}$(C), $LaMn_{0.5}Co_{0.5}O_{3+\delta}$(D), $La_{0.8}Sr_{0.2}Mn_{0.5}Co_{0.5}O_{3+\delta}$(E), and $La_{0.6}Sr_{0.4}Mn_{0.5}Co_{0.5}O_{3+\delta}$(F) in the water splitting stage at 850 ℃.

decreased with the Sr doping amount, since the doping of Co promotes the cracking reaction of methane, producing more excess H_2. However, the introduction of Sr inhibits the formation of carbon and reduces the amount of excess H_2. The H_2/CO in methane reforming stage was close to 2 for all the oxygen carriers, as there is no carbon deposition in this period.

It can be observed from Fig. 8(a) that the methane conversion in the

methane reforming period for the $LaMn_{0.7}Co_{0.3}O_{3+\delta}$, $LaMn_{0.5}Co_{0.5}O_{3+\delta}$ and $La_{0.8}Sr_{0.2}Mn_{0.5}Co_{0.5}O_{3+\delta}$ were about the same, higher than other perovskites. According to Fig. 8(b), the $LaMn_{0.7}Co_{0.3}O_{3+\delta}$ and $La_{0.8}Sr_{0.2}Mn_{0.5}Co_{0.5}O_{3+\delta}$ possessed higher CO selectivity than $LaMn_{0.5}Co_{0.5}O_{3+\delta}$. The yield of the effective syngas of $La_{0.8}Sr_{0.2}Mn_{0.5}Co_{0.5}O_{3+\delta}$ was more than that of $LaMn_{0.7}Co_{0.3}O_{3+\delta}$. Comprehensively considering the various properties, $La_{0.8}Sr_{0.2}Mn_{0.5}Co_{0.5}O_{3+\delta}$ possessed the best performance for CLSMR as a whole. In addition, the performance of $LaMn_{0.6}Co_{0.4}O_{3+\delta}$, $La_{0.7}Sr_{0.3}Mn_{0.5}Co_{0.5}O_{3+\delta}$ and $La_{0.8}Sr_{0.2}Mn_{0.7}Co_{0.3}O_{3+\delta}$ oxygen carrier was investigated in order to understand the best substitution proportion of Co and Sr, as displayed in Fig. S4–S6. According to the comparison of $La_{0.8}Sr_{0.2}Mn_{0.7}Co_{0.3}O_{3+\delta}$ and $La_{0.8}Sr_{0.2}Mn_{0.5}Co_{0.5}O_{3+\delta}$ shown in Fig. S6, the carbon deposition of $La_{0.8}Sr_{0.2}Mn_{0.7}Co_{0.3}O_{3+\delta}$ occurs later, the yield of the effective syngas and CO selectivity are similar, while the methane conversion is much lower than $La_{0.8}Sr_{0.2}Mn_{0.5}Co_{0.5}O_{3+\delta}$. Combine the performance $LaMn_{0.6}Co_{0.4}O_{3+\delta}$ and $La_{0.7}Sr_{0.3}Mn_{0.5}Co_{0.5}O_{3+\delta}$, it can be deduced that the best substitution proportion of Co and Sr could be set in range of 0.4–0.5 and 0.2–0.4, respectively.

Fig. 9 illustrates the yield of the produced gas for the perovskites in the water splitting stage. According to Fig. 9, all the hydrogen generated from the $LaMnO_{3+\delta}$ perovskite was originated from the oxidation of oxygen carrier (R4). The hydrogen of other perovskites was generated from the carbon gasification (R6 and R2) in addition to the oxidation of oxygen carrier. For the Co doped perovskites, the yield of hydrogen from the oxidation of oxygen carrier increased obviously with the cobalt-doping amount, deducing that the introduction of Co could improve the oxygen uptaking capacity of the $LaMnO_{3+\delta}$ perovskites and increase the hydrogen yield in the water splitting stage, originating from more oxygen releases in the methane conversion stage (Fig. 7). The yield of hydrogen from oxidation of oxygen carrier of the three $La_{1-x}Sr_xMn_{0.5}Co_{0.5}O_{3+\delta}$ perovskites declined slightly with the Sr content, suggesting that the doping of Sr results in the decrease of the oxygen

Fig. 10. The yield of the produced gas (a), methane conversion, CO selectivity, H_2/CO in the methane conversion stage (b) and the yield of the produced gas in the water splitting stage (c) of $La_{0.8}Sr_{0.2}Mn_{0.5}Co_{0.5}O_{3+\delta}$ perovskite in the cyclic tests.
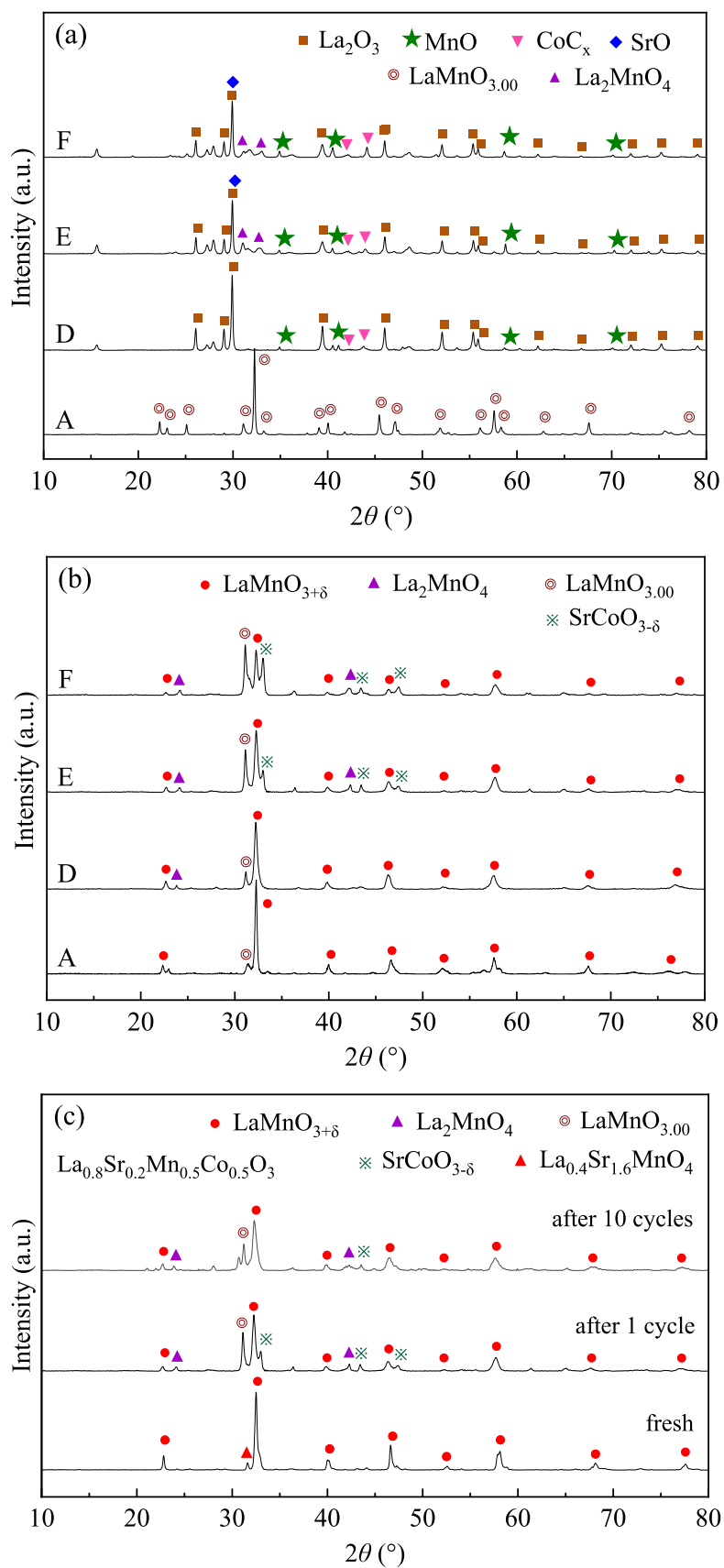
Fig. 11. XRD patterns of LaMnO$_{3+\delta}$(A), LaMn$_{0.5}$Co$_{0.5}$O$_{3+\delta}$(D), La$_{0.8}$Sr$_{0.2}$Mn$_{0.5}$Co$_{0.5}$O$_{3+\delta}$(E), La$_{0.6}$Sr$_{0.4}$Mn$_{0.5}$Co$_{0.5}$O$_{3+\delta}$(F) at reduced (a) and oxidized (b) state in the 1st cycle and La$_{0.8}$Sr$_{0.2}$Mn$_{0.5}$Co$_{0.5}$O$_{3+\delta}$ in fresh and after 1st, 10th cycle (c).

uptaking capacity corresponding to the lessening of the oxygen releasing amount shown in Fig. 7. The yield of H_2, CO and CO_2 from carbon gasification increased with the Co content for $LaMn_{1-y}Co_yO_{3+\delta}$, while decreased with the Sr substitution proportion for $La_{1-x}Sr_xMn_{0.5}Co_{0.5}O_{3+\delta}$. This is on account of the corresponding variation of the amount of carbon deposition depicted in Fig. S1.

3.3. Redox performance of $La_{0.8}Sr_{0.2}Mn_{0.5}Co_{0.5}O_{3+\delta}$ oxygen carrier in cyclic tests

As mentioned above, $La_{0.8}Sr_{0.2}Mn_{0.5}Co_{0.5}O_{3+\delta}$ possessed the best performance for CLSMR as a whole. Therefore, $La_{0.8}Sr_{0.2}Mn_{0.5}Co_{0.5}O_{3+\delta}$ is chosen as a representative to evaluate the cyclic performance of $La_{1-x}Sr_xMn_{1-y}Co_yO_{3+\delta}$ perovskites. The Redox performance of $La_{0.8}Sr_{0.2}Mn_{0.5}Co_{0.5}O_{3+\delta}$ perovskite in cyclic tests is presented in Figs. 10, S7 and S8.

Fig. 10(a) shows the yield of CO_2, CO and H_2 of $La_{0.8}Sr_{0.2}Mn_{0.5}Co_{0.5}O_{3+\delta}$ perovskite in the methane conversion stage in cyclic tests. As observed in Fig. 10(a), the yield of CO_2 decreased slightly with the cyclic process, which is attributed to that the unselective oxygen releasing in the methane conversion stage cannot replenish completely (Fig. 12). The yield of CO and H_2 approximately maintained a constant in the cyclic tests. The average yield of CO and H_2 were 1.49 mmol g^{-1} and 2.93 mmol g^{-1}, respectively, and the average syngas yield was 4.42 mmol g^{-1}. This indicates that the syngas could be produced stably in continuous redox process, in virtue of that the selective oxygen could release and uptake with a constant amount. It can be observed from Fig. 10 (b) that the methane conversion was in range of 52.2–60.8% and the average conversion was 55.2%. The CO selectivity of the oxygen carrier rose slightly from 79.1% to 86.0% (83.7% on average) in the cyclic test due to the decrease of the CO_2 yield shown in Fig. 10(a). The H_2/CO approximately maintained 2 in the methane conversion stage during the 10 cyclic tests, indicating that high-quality syngas could be produced and no carbon formation occur in successive redox process. Fig. 10(b) suggests relatively high and stable reactivity, syngas selectivity and resistance towards carbon deposition of $La_{0.8}Sr_{0.2}Mn_{0.5}Co_{0.5}O_{3+\delta}$ oxygen carrier in cyclic redox process. Fig. 10 (c) illustrates the hydrogen yield of $La_{0.8}Sr_{0.2}Mn_{0.5}Co_{0.5}O_{3+\delta}$ perovskite in the water splitting stage of cyclic process. It can be observed that pure hydrogen could be generated without the impurity of CO_2 and CO. The yield of hydrogen nearly kept stable with an average yield of 2.48 mmol g^{-1}, which means that pure hydrogen could be produced stably in the continuous redox process via $La_{0.8}Sr_{0.2}Mn_{0.5}Co_{0.5}O_{3+\delta}$ oxygen carrier.

3.4. Characterization of $La_{1-x}Sr_xMn_{1-y}Co_yO_{3+\delta}$ perovskites after redox tests

XRD characterizations were conducted to investigate the evolution of phases of the perovskites during or after cyclic tests, as shown in Fig. 11. Fig. 11(a) illustrates the XRD patterns of the oxygen carrier samples after reduction in the 1st cycle. It can be seen that only $LaMnO_{3.00}$ (#35-1353) appeared in the reduced $LaMnO_{3+\delta}$ sample, suggesting that the $LaMnO_{3+\delta}$ remained perovskite structure after removing part lattice oxygen. The peaks of La_2O_3 (#50-0602), MnO (#07-0230) and CoC_x (several crystal types) were observed in the diffraction patterns of the $LaMn_{0.5}Co_{0.5}O_{3+\delta}$, $La_{0.8}Sr_{0.2}Mn_{0.5}Co_{0.5}O_{3+\delta}$ and $La_{0.6}Sr_{0.4}Mn_{0.5}Co_{0.5}O_{3+\delta}$ samples, which indicates that these perovskites suffers phase decomposition in the methane conversion stage. CoC_x was found which originates from the reaction of metallic Co^0 and high active atomic carbon generated from methane decomposition. The peaks of carbon were not observed, suggesting that other carbon forming in the methane conversion stage may be amorphous rather than graphitic. SrO (#06-0520) and La_2MnO_4 (#33-0897) were also detected in the patterns of $La_{0.8}Sr_{0.2}Mn_{0.5}Co_{0.5}O_{3+\delta}$ and $La_{0.6}Sr_{0.4}Mn_{0.5}Co_{0.5}O_{3+\delta}$ samples. For the oxygen carriers at oxidation state after the 1st cycle as shown in Fig. 11(b), peaks of $LaMnO_{3+\delta}$ (#51-
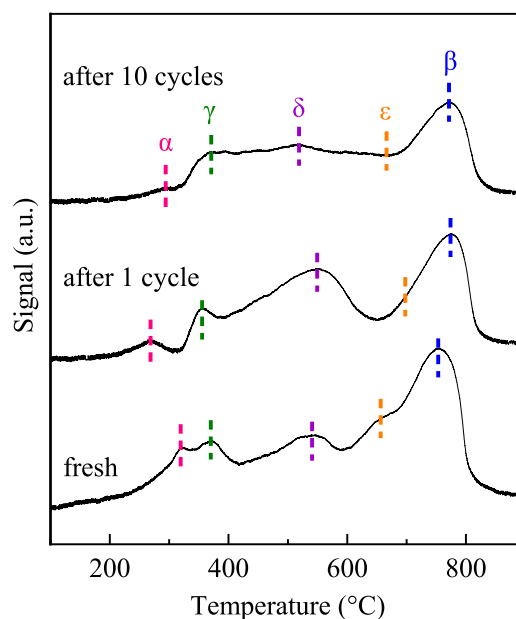

Fig. 12. H_2-TPR profiles of $La_{0.8}Sr_{0.2}Mn_{0.5}Co_{0.5}O_{3+\delta}$ oxygen carrier in fresh and after the 1st, 10th cycle.

1516) perovskite and an extremely weak peak of $LaMnO_{3.00}$ (#35-1353) was observed in the pattern of $LaMnO_{3+\delta}$ sample, suggesting that the reduced perovskite recovers to the $LaMnO_{3+\delta}$ form. For the oxidized $LaMn_{0.5}Co_{0.5}O_{3+\delta}$, $La_{0.8}Sr_{0.2}Mn_{0.5}Co_{0.5}O_{3+\delta}$ and $La_{0.6}Sr_{0.4}Mn_{0.5}Co_{0.5}O_{3+\delta}$ samples, the characteristic peaks of $LaMnO_{3+\delta}$ (#51-1516) perovskite was dominating and peaks of $LaMnO_{3.00}$ (#35-1353) and La_2MnO_4 (#33-0897) perovskite with weak intensity were also found, indicating that all the single oxides combines into the original perovskites, which means good regenerability of $La_{1-x}Sr_xMn_{1-y}Co_yO_{3+\delta}$ oxygen carriers. The $SrCoO_3$ (#38-1148) was observed in the $La_{0.8}Sr_{0.2}Mn_{0.5}Co_{0.5}O_{3+\delta}$ and $La_{0.6}Sr_{0.4}Mn_{0.5}Co_{0.5}O_{3+\delta}$ samples and the peak intensity of $SrCoO_3$ and $LaMnO_{3.00}$ was enhanced with the Sr doping amount. Fig. 11(c) illustrates the patterns of $La_{0.8}Sr_{0.2}Mn_{0.5}Co_{0.5}O_{3+\delta}$ samples in fresh and after the 1st, the 10th cycle. The main peaks were corresponding to $LaMnO_{3+\delta}$ (#51-1516) perovskite in the sample at oxidation state after the first cycle. Compared with the fresh sample, $LaMnO_{3.00}$, La_2MnO_4 and $SrCoO_3$ perovskites formed, which is attributed to that H_2O cannot oxidize the single oxide into the original perovskite on account of its relatively weak oxidizability. The intensity of the peaks from $LaMnO_{3.00}$, La_2MnO_4 and $SrCoO_3$ weakened after the cyclic tests compared with the sample after the 1st cycle. The pattern of the sample after the 10th cycle was almost the same as that after the 1st cycle, which means good stability of $La_{0.8}Sr_{0.2}Mn_{0.5}Co_{0.5}O_{3+\delta}$ oxygen carrier.

Fig. 12 shows the H_2-TPR profiles of $La_{0.8}Sr_{0.2}Mn_{0.5}Co_{0.5}O_{3+\delta}$ oxygen carrier in fresh and after the 1st, 10th cycle. The reduction profiles exhibit five peaks which are the same as those in Fig. 4. For the oxygen carrier after the first cycle, it can be observed that the area of peak α decreased compared with that in the fresh sample, resulting from that less Mn^{4+} was generated in the water splitting stage attributed to the relatively weak oxidizability of H_2O. The area of peaks γ and δ were approximately equal to that of the fresh sample while the area of peaks ε and β decreased in contrast to that in the fresh one. For the sample after 20 cycles, the area of peak α and γ decreased slightly compared with that after one cycle. The peak δ exhibited a weak intensity and a long temperature range, and overlapped with the peak ε. These probably results from that sintering of the oxygen carrier particles prevents the replenishment of part of oxygen in the water splitting stage. The temperature of each peak is basically constant in the three profiles, indicating that the activity of the oxygen is changeless during the cyclic tests. Approximately identical reduction profiles after 1 and 10 cycles suggests good
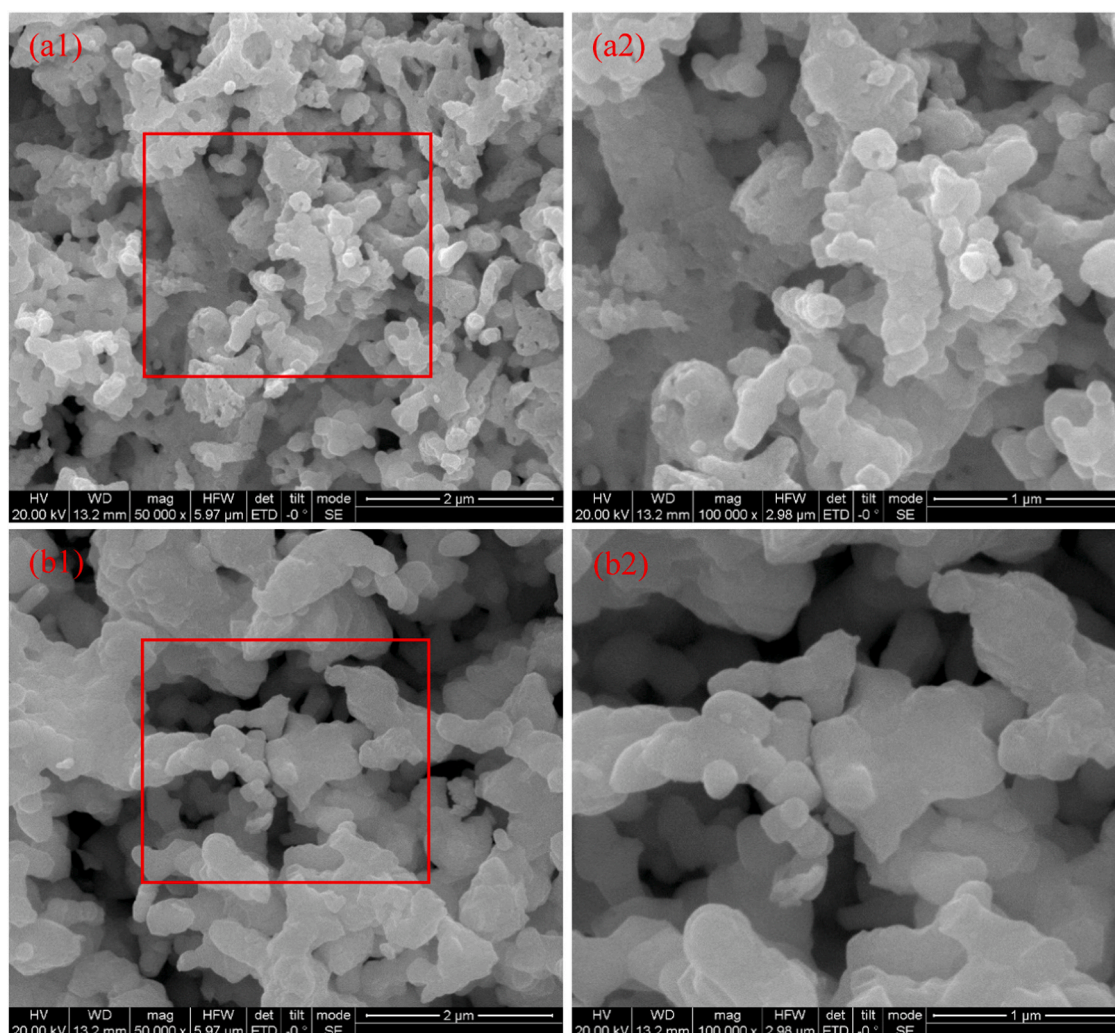
Fig. 13. SEM images of $La_{0.8}Sr_{0.2}Mn_{0.5}Fe_{0.5}O_{3+\delta}$ oxygen carriers in fresh (a1, a2) and after 10 cycles (b1, b2). ((a2) and (b2) are the enlargement of the image in the box in (a1) and (b1), respectively). (For interpretation of the references to color in this figure legend, the reader is referred to the web version of this article.).

stability of $La_{0.8}Sr_{0.2}Mn_{0.5}Co_{0.5}O_{3+\delta}$ oxygen carrier.

SEM was performed to determine the micromorphology of the perovskite sample during the redox cycles and the SEM images are shown in Fig. 13. It can be seen that the fresh sample and the one after cycles both exhibited the grains bonded together slightly, suggesting light sintering after calcination and redox process in high temperature. The morphologies in Fig. 13 (b1) and (b2) showed more pores and larger gaps on the surface of the particles compared with Fig. 13 (a1) and (a2). The interconnected pores and gaps on the surface of the particles avails to the penetration and diffusion of reactant gas into the solid particles [40]. The morphology of the reacted sample was not substantially changed [4,21,40] and the porous structure on the surface of the oxygen carrier particles was improved compared with the fresh sample. This deduces good thermal stability and resistance towards sintering of the $La_{0.8}Sr_{0.2}Mn_{0.5}Co_{0.5}O_{3+\delta}$ perovskite in the successive alternating reducing and oxidizing process.

3.5. Double adjustment of Co and Sr for the $LaMnO_{3+\delta}$ perovskite

For the partial oxidation of $LaMnO_{3+\delta}$ perovskite in the methane conversion stage, the methane molecule may be activated at the oxygen vacancies on the surface of the perovskite particles and is then oxidized into CO and H_2 by the selective lattice oxygen migrating from the bulk of the perovskite particles, as shown in Fig. 14(a). The oxygen vacancies are low active and lead to a low rate of methane activation, low

reactivity of methane partial oxidation (Fig. 8(a)) and low syngas yield (Fig. 7). In this case, the oxygen anion migration rate in the bulk is higher than the activation rate of methane molecule on the surface of the oxygen carrier particles, the supply of lattice oxygen outwards in the oxygen carrier particles is sufficient and all the activated methane could be oxidized into syngas, just like the partial oxidation period of $LaMnO_{3+\delta}$ as shown in Fig. 6(a).

In the Co doped $LaMnO_{3+\delta}$ perovskite as depicted in Fig. 14 (b), Co cations or atoms is another kind of surface active site at which the methane molecules are activated. As surface active site with high activity, the presence of Co greatly facilitated the activation and adsorption of methane molecules [41], increasing the oxygen release rate. As a result, the productive rate of syngas increased dramatically with the Co substitution proportion (Fig. 6(b)–(d)). In addition, several other minor reasons also improve the release of the oxygen. The activity of the selective oxygen combining with Co^{2+} is higher than that with Mn^{3+} (Fig. 4), and the higher Co content increases the release rate of selective oxygen. The substitution of Mn^{3+} by Co^{2+} could result in the formation oxygen vacancies after Mn^{4+} is reduced into Mn^{3+} (After the non-stoichiometric excess oxygen is exhausted as mentioned in Section 3.1). The oxygen vacancies could facilitate the migration of oxygen anion [41] and enhance the release of oxygen (Fig. 4). The structure of the perovskite evolved from hexagonal to orthorhombic (Table 1) resulting from the incorporation of Co into the $LaMnO_{3+\delta}$ perovskite lattice. This weakens the bound of the lattice to the mobility of oxygen
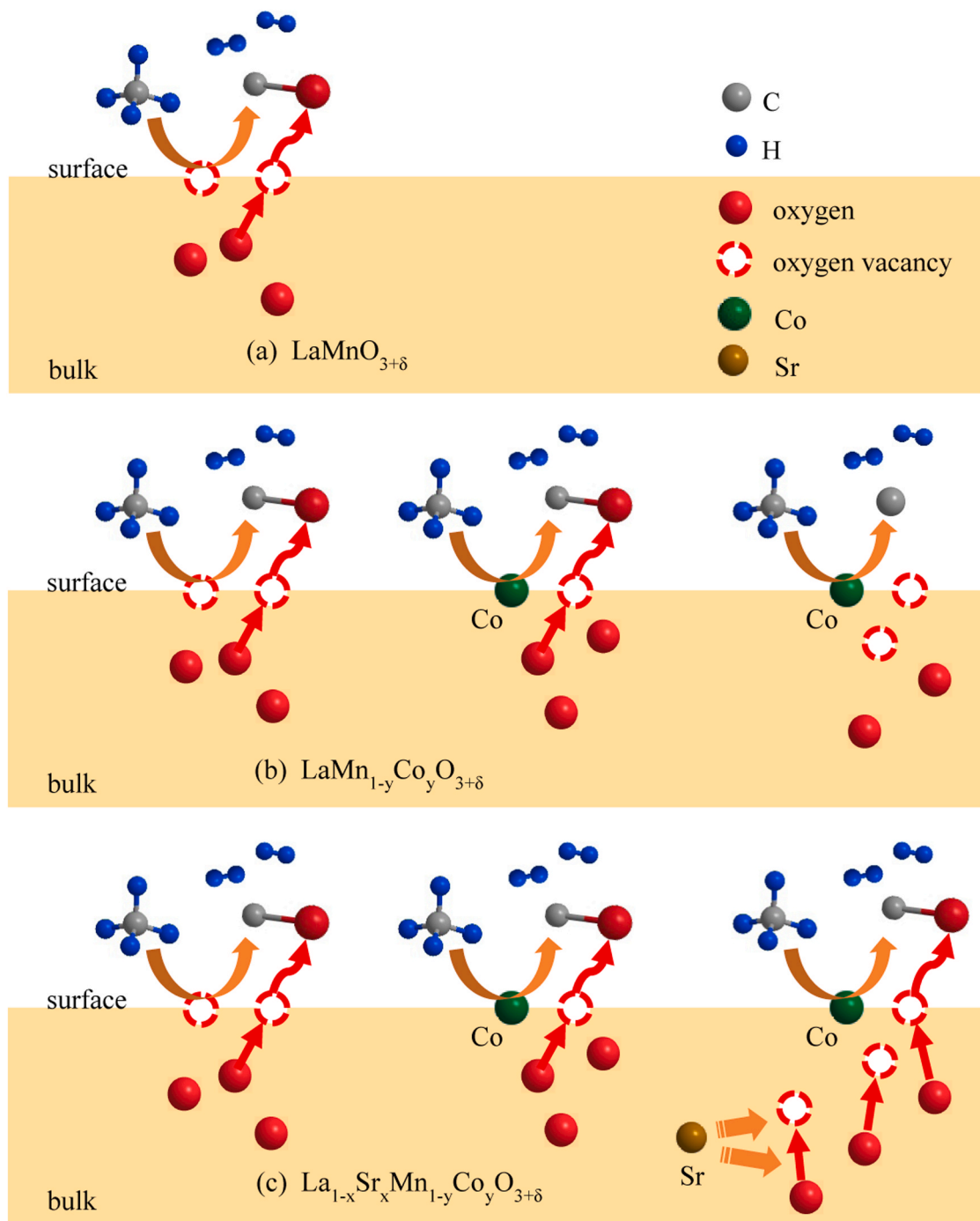
Fig. 14. the effect of Co and Sr doping on the partial oxidation of LaMnO$_{3+\delta}$ perovskite.

[42], decreases the oxygen vacancy formation energy [15], and accelerates the oxygen migration. However, these factors are not the main ones, and the effect of Co doping on the methane activation is greater than the oxygen anion transmission since the variation of carbon formation is much more obvious than that of CO productive rate according to Fig. 6(a)–(d). In this situation, the transmission rate of lattice oxygen in the interior is lower than the activation rate of methane on the surface of the perovskite particles. As a result, only part of the activated methane could be selectively oxidized into syngas, the other part would convert into carbon, just like the carbon deposition period of all cobalt-doping oxygen carriers. Carbon deposition occurs in case of insufficient supply of lattice oxygen. When the supply of available oxygen cannot satisfy the need of partial oxidation of methane, activated

methane decomposes into adsorbed atomic carbon on Co^0 atom or Co cation. The atomic carbon which is unstable could further aggregate into carbon fibers or combine with metallic Co^0 to form CoC$_x$ (Fig. 11) on the surface of perovskite particles at high temperature [43,44]. The promotion of the methane activation originating from Co doping enhances the reactivity of the perovskites (Fig. 8(a)) but leads to early occurrence of carbon formation (Fig. 6(b)–(d)) which worsens the quality of syngas (Fig. 8(c)) and decreases the yield of effective syngas (Fig. 7).

On the other hand, as shown in Fig. 14 (c), the substitution of La^{3+} by Sr^{2+} leads to the increase of oxygen vacancies to compensate for the decrease of positive charge (Fig. S3). The oxygen vacancies facilitated the migration of oxygen anion and the release of selective oxygen, which is corresponding to the decrease of the temperature of peaks ε and β with

the Sr-doping proportion of $La_{1-x}Sr_xMn_{0.5}Co_{0.5}O_{3+\delta}$ in Fig. 4. The improvement of the conduction of oxygen ion and the oxygen release promotes the generation of syngas, increasing the maximum of component of CO (Fig. 6(e) and (f)) or causing the maximum of component of CO appear earlier (Fig. 6(f)). Furthermore, the enhancement of the oxygen ion conduction and the release of selective oxygen improves the supply of lattice oxygen from the bulk to the surface of particles, restraining the occurrence of carbon deposition. The doping of Sr delays the occurrence of carbon deposition (Fig. 6(e) and (f)), increasing the yield of effective syngas (Fig. 7) and remaining high reactivity of oxygen carriers in the methane reforming period (Fig. 8(a)).

Therefore, the double adjustment of Co and Sr is beneficial to the matching of the transmission rate of oxygen anion in the interior and the activation rate of methane on the surface of the perovskite particles, accomplishing both high reactivity and resistance of carbon deposition.

4. Conclusion

In summary, the doping of Co and Sr has the capability of adjusting the properties of the $La_{1-x}Sr_xMn_{1-y}Co_yO_{3+\delta}$ perovskites. Co cations provided surface active sites which promoted the methane activation on the surface of the oxygen carrier particles. As a result, the yield of CO_2 and syngas, the methane conversion, the molar ratio of H_2/CO and the amount of carbon deposition increased while the CO selectivity declined with the Co substitution amount. Furthermore, the doping of Co caused the carbon formation to occur earlier and shortened the period of methane reforming, leading to the decrease of the yield of usable syngas. On the other hand, the Sr doping increased the oxygen vacancies and enhanced the oxygen anion migration rate. Meanwhile, the Sr cations inhibited the activation and adsorption of methane. Therefore, the introduction of Sr cations lowered the CO_2 yield, the amount of carbon deposition and H_2/CO, while increased the CO selectivity. The Sr doping also delayed the occurrence of carbon formation, lengthened the methane reforming period, and increasing the yield of effective syngas.

The main effect of Co doping was the acceleration of methane activation on the surface, while Sr doping enhanced the conduction of oxygen anion. Therefore, the appropriate doping proportion of Co and Sr was beneficial to the matching of the oxygen anion conduction of in the bulk and the methane activation on the surface of the perovskite particles. The substitution proportion of Co and Sr could be set in range of 0.4–0.5 and 0.2–0.4, respectively. The $La_{0.8}Sr_{0.2}Mn_{0.5}Co_{0.5}O_{3+\delta}$ perovskite could produce high-quality syngas with the H_2/CO of 2, the yield of 4.42 mmol g^{-1}, methane conversion of 55.2%, CO selectivity of 83.7% and pure hydrogen with the yield of 2.48 mmol g^{-1} in the continuous redox process. The $La_{0.8}Sr_{0.2}Mn_{0.5}Co_{0.5}O_{3+\delta}$ perovskite possessed good stability in the cyclic redox test.

CRediT authorship contribution statement

Xianglei Yin: Conceptualization, Investigation, Methodology, Data curation, Writing – original draft. **Laihong Shen:** Resources, Methodology, Validation, Writing – review & editing, Supervision, Project administration, Funding acquisition. **Shen Wang:** Investigation, Writing – review & editing. **Baoyi Wang:** Writing – review & editing. **Cheng Shen:** Writing – review & editing.

Declaration of Competing Interest

We declare that we have no known competing financial interests or personal relationships that could have appeared to influence the work reported in this paper.

Acknowledgments

Appendix A. Supporting information

Supplementary data associated with this article can be found in the online version at doi:10.1016/j.apcatb.2021.120816.

References

[1] A. Löfberg, T. Kane, J. Guerrero-Caballero, L. Jalowiecki-Duhamel, Chemical looping dry reforming of methane: toward shale-gas and biogas valorization, Chem. Eng. Process. Process Intensif. 122 (2017) 523–529.

[2] D. Kang, H.S. Lim, M. Lee, J.W. Lee, Syngas production on a Ni-enhanced Fe_2O_3/Al_2O_3 oxygen carrier via chemical looping partial oxidation with dry reforming of methane, Appl. Energy 211 (2018) 174–186.

[3] K. Li, H. Wang, Y. Wei, D. Yan, Partial oxidation of methane to syngas with air by lattice oxygen transfer over ZrO_2-modified Ce–Fe mixed oxides, Chem. Eng. J. 173 (2011) 574–582.

[4] K. Zhao, F. He, Z. Huang, G. Wei, A. Zheng, H. Li, Z. Zhao, Perovskite-type oxides $LaFe_{1-x}Co_xO_3$ for chemical looping steam methane reforming to syngas and hydrogen co-production, Appl. Energy 168 (2016) 193–203.

[5] S. Ma, S. Chen, A. Soomro, W. Xiang, Effects of supports on hydrogen production and carbon deposition of Fe-based oxygen carriers in chemical looping hydrogen generation, Int. J. Hydrog. Energy 42 (2017) 11006–11016.

[6] H.R. Forutan, E. Karimi, A. Hafizi, M.R. Rahimpour, P. Keshavarz, Expert representation chemical looping reforming: a comparative study of Fe, Mn, Co and Cu as oxygen carrier supported on Al_2O_3, J. Ind. Eng. Chem. 21 (2015) 900–911.

[7] D. Hosseini, P.M. Abdala, F. Donat, S.M. Kim, C.R. Müller, Bifunctional core-shell architecture allows stable H_2 production utilizing CH_4 and CO_2 in a catalytic chemical looping process, Appl. Catal. B Environ. 258 (2019), 117946.

[8] S. Ma, S. Chen, A. Soomro, W. Xiang, Effects of CeO_2, ZrO_2, and Al_2O_3 supports on iron oxygen carrier for chemical looping hydrogen generation, Energy Fuel 31 (2017) 8001–8013.

[9] Y. Wang, Y. Zheng, Y. Wang, H. Wang, X. Zhu, Y. Wei, Y. Wang, L. Jiang, Z. Yang, K. Li, Evaluation of Fe substitution in perovskite $LaMnO_3$ for the production of high purity syngas and hydrogen, J. Power Sources 449 (2020), 227505.

[10] X. Zhu, Y. Wei, H. Wang, K. Li, Ce–Fe oxygen carriers for chemical-looping steam methane reforming, Int. J. Hydrog. Energy 38 (2013) 4492–4501.

[11] K. Zhao, A. Zheng, H. Li, F. He, Z. Huang, G. Wei, Y. Shen, Z. Zhao, Exploration of the mechanism of chemical looping steam methane reforming using double perovskite-type oxides $La_{1.6}Sr_{0.4}FeCoO_6$, Appl. Catal. B Environ. 219 (2017) 672–682.

[12] O. Mihai, D. Chen, A. Holmen, Chemical looping methane partial oxidation: the effect of the crystal size and O content of $LaFeO_3$, J. Catal. 293 (2012) 175–185.

[13] M. VANDENBOSSCHE, S. MCINTOSH, The rate and selectivity of methane oxidation over $La_{0.75}Sr_{0.25}Cr_xMn_{1-x}O_{3-\delta}$ as a function of lattice oxygen stoichiometry under solid oxide fuel cell anode conditions, J. Catal. 255 (2008) 313–323.

[14] M. Tang, L. Xu, M. Fan, Progress in oxygen carrier development of methane-based chemical-looping reforming: A review, Appl. Energy 151 (2015) 143–156.

[15] X. Zhu, K. Li, L. Neal, F. Li, Perovskites as geo-inspired oxygen storage materials for chemical looping and three-way catalysis: a perspective, ACS Catal. 8 (2018) 8213–8236.

[16] K. Zhao, F. He, Z. Huang, A. Zheng, H. Li, Z. Zhao, Three-dimensionally ordered macroporous $LaFeO_3$ perovskites for chemical-looping steam reforming of methane, Int. J. Hydrog. Energy 39 (2014) 3243–3252.

[17] F. He, J. Chen, S. Liu, Z. Huang, G. Wei, G. Wang, Y. Cao, K. Zhao, $La_{1-x}Sr_xFeO_3$ perovskite-type oxides for chemical-looping steam methane reforming: identification of the surface elements and redox cyclic performance, Int. J. Hydrog. Energy 44 (2019) 10265–10276.

[18] Y. Shen, K. Zhao, F. He, H. Li, The structure-reactivity relationships of using three-dimensionally ordered macroporous $LaFe_{1-x}Ni_xO_3$ perovskites for chemical-looping steam methane reforming, J. Energy Inst. 92 (2019) 239–246.

[19] L. Nalbandian, A. Evdou, V. Zaspalis, $La_{1-x}Sr_xM_yFe_{1-y}O_{3-\delta}$ perovskites as oxygen-carrier materials for chemical-looping reforming, Int. J. Hydrog. Energy 36 (2011) 6657–6670.

[20] M. Rydén, A. Lyngfelt, T. Mattisson, D. Chen, A. Holmen, E. Bjørgum, Novel oxygen-carrier materials for chemical-looping combustion and chemical-looping reforming; $La_xSr_{1-x}Fe_yCo_{1-y}O_{3-\delta}$ perovskites and mixed-metal oxides of NiO, Fe_2O_3 and Mn_3O_4, Int. J. Greenh. Gas Control 2 (2008) 21–36.

[21] Z. Kun, H. Fang, H. Zhen, Z. Anqing, $La_{1-x}Sr_xFeO_3$ perovskites as oxygen carriers for the partial oxidation of methane to syngas, Chin. J. Catal. 35 (2014) 1196–1205.

[22] X. Yin, S. Wang, B. Wang, L. Shen, Perovskite-type $LaMn_{1-x}B_xO_{3+\delta}$ (B=Fe, CO and Ni) as oxygen carriers for chemical looping steam methane reforming, Chem. Eng. J. 422 (2021), 128751.

[23] R.V. Krishnan, A. Banerjee, Evidence of dynamic Jahn-Teller effects in ferromagnetism of rhombohedral Al-substituted lanthanum manganite, J. Phys. Condens. Matter 12 (2000) 3835–3847.

[24] A.J.L.A. Hend Najjar, A.H. Batisbc, Combustion synthesis of $LaMn_{1-x}Al_xO_{3+\delta}$ (0≤x≤1): tuning catalytic properties for methane deep oxidation, Catal. Sci. Technol. 3 (2013) 1002–1016.

[25] S. Cimino, L. Lisi, S. De Rossi, M. Faticanti, P. Porta, Methane combustion and CO oxidation on LaAl$_{1-x}$Mn$_x$O$_3$ perovskite-type oxide solid solutions, Appl. Catal. B Environ. 43 (2003) 397–406.

[26] M. Ghiasi, M.U. Delgado-Jaime, A. Malekzadeh, R. Wang, P.S. Miedema, M. Beye, F.M.F. de Groot, Mn and Co charge and spin evolutions in LaMn$_{1-x}$Co$_x$O$_3$ nanoparticles, J. Phys. Chem. C 120 (2016) 8167–8174.

[27] M. Pishahang, E. Bakken, S. Stølen, Y. Larring, C.I. Thomas, Oxygen non-stoichiometry and redox thermodynamics of LaMn$_{1-x}$Co$_x$O$_{3-\delta}$, Solid State Ion. 231 (2013) 49–57.

[28] J. Hu, J. Ma, L. Wang, H. Huang, L. Ma, Preparation, characterization and photocatalytic activity of Co-doped LaMnO$_3$/graphene composites, Powder Technol. 254 (2014) 556–562.

[29] J. Wang, Y. Su, X. Wang, J. Chen, Z. Zhao, M. Shen, The effect of partial substitution of Co in LaMnO$_3$ synthesized by sol–gel methods for NO oxidation, Catal. Commun. 25 (2012) 106–109.

[30] R. Ran, X. Wu, D. Weng, J. Fan, Oxygen storage capacity and structural properties of Ni-doped LaMnO$_3$ perovskites, J. Alloy Compd. 577 (2013) 288–294.

[31] V.R.M. Melo, R.L.B.A. Medeiros, R.M. Braga, H.P. Macedo, J.A.C. Ruiz, G.T. Moure, M.A.F. Melo, D.M.A. Melo, Study of the reactivity of double-perovskite type oxide La$_{1-x}$M$_x$NiO$_4$ (M=Ca or Sr) for chemical looping hydrogen production, Int. J. Hydrog. Energy 43 (2018) 1406–1414.

[32] A. Cyza, A. Kopia, A. Cieniek, J. Kusiński, Structural Characterization of Sr Doped LaFeO$_3$ Thin Films Prepared By Pulsed Electron Deposition Method. Materials today, proceedings 3 (2016) 2707–2712.

[33] K. Zhao, F. He, Z. Huang, G. Wei, A. Zheng, H. Li, Z. Zhao, Perovskite-type LaFe$_{1-x}$Mn$_x$O$_3$ (x=0, 0.3, 0.5, 0.7, 1.0) oxygen carriers for chemical-looping steam methane reforming: Oxidation activity and resistance to carbon formation, Korean J. Chem. Eng. 34 (2017) 1651–1660.

[34] J.M. Córdoba, M. Ponce, M.J. Sayagués, Structure evolution in the LaMn$_{1-x}$Fe$_x$O$_{3+\delta}$ system by Rietveld analysis, Solid State Ion. 303 (2017) 132–137.

[35] J.X. Flores-Lasluisa, F. Huerta, D. Cazorla-Amorós, E. Morallón, Structural and morphological alterations induced by cobalt substitution in LaMnO$_3$ perovskites, J. Colloid Interface Sci. 556 (2019) 658–666.

[36] Y. Zheng, K. Li, H. Wang, D. Tian, Y. Wang, X. Zhu, Y. Wei, M. Zheng, Y. Luo, Designed oxygen carriers from macroporous LaFeO$_3$ supported CeO$_2$ for chemical-looping reforming of methane, Appl. Catal. B Environ. 202 (2017) 51–63.

[37] B. Savova, D. Filkova, D. Crişan, M. Crişan, M. Räileanu, N. Drăgan, A. Galtayries, J.C. Védrine, Neodymium doped alkaline-earth oxide catalysts for propane oxidative dehydrogenation. Part I. Catalyst characterisation, Appl. Catal. A Gen. 359 (2009) 47–54.

[38] C. Zhang, Y. Guo, Y. Guo, G. Lu, A. Boreave, L. Retailleau, A. Baylet, A. Giroir-Fendler, LaMnO$_3$ perovskite oxides prepared by different methods for catalytic oxidation of toluene, Appl. Catal. B Environ. 148–149 (2014) 490–498.

[39] O. Mihai, D. Chen, A. Holmen, Catalytic consequence of oxygen of lanthanum ferrite perovskite in chemical looping reforming of methane, Ind. Eng. Chem. Res. 50 (2011) 2613–2621.

[40] F. He, X. Li, K. Zhao, Z. Huang, G. Wei, H. Li, The use of La$_{1-x}$Sr$_x$FeO$_3$ perovskite-type oxides as oxygen carriers in chemical-looping reforming of methane, Fuel 108 (2013) 465–473.

[41] A. Shafiefarhood, J.C. Hamill, L.M. Neal, F. Li, Methane partial oxidation using FeO$_x$@La$_{0.8}$Sr$_{0.2}$FeO$_{3-\delta}$ core-shell catalyst – transient pulse studies, Phys. Chem. Chem. Phys. 17 (2015) 31297–31307.

[42] N.G.F.H. Amit Mishra, Perovskite-structured AMn$_x$B$_{1-x}$O$_3$(A=Ca or Ba; B=Fe or Ni) redox catalysts for partial oxidation of methane, Catal. Sci. Technol. 6 (2016) 4535–4544.

[43] X. Yin, S. Wang, R. Sun, S. Jiang, L. Shen, A Ce–Fe oxygen carrier with a core–shell structure for chemical looping steam methane reforming, Ind. Eng. Chem. Res. 59 (2020) 9775–9786.

[44] C.H. Bartholomew, Mechanisms of catalyst deactivation, Appl. Catal. A Gen. 212 (2001) 17–60.